

Generating Exceptional Knots and Links with Arbitrary Braiding Topology

Bin Jiang,^{1,2} Aolong Guo,^{3,2} Qilin Cai,^{2,4,*} and Jian-Hua Jiang^{5,1,4,6,†}

¹*Department of Modern Physics, School of Physical Sciences,
University of Science and Technology of China, Hefei, 230026, China*

²*Suzhou Institute for Advanced Research, University of Science and Technology of China, Suzhou, 215123, China*

³*Department of Physics, School of Physical Sciences, University of Science and Technology of China, Hefei, 230026, China*

⁴*School of Biomedical Engineering, Division of Life Sciences and Medicine,
University of Science and Technology of China, Hefei 230026, China*

⁵*State Key Laboratory of Bioinspired Interfacial Materials Science, Suzhou Institute for Advanced Research,
University of Science and Technology of China, Suzhou, 215123, China*

⁶*School of Physical Science and Technology & Collaborative Innovation Center of
Suzhou Nano Science and Technology, Soochow University, Suzhou 215006, China*

(Dated: March 5, 2026)

Non-Hermitian systems support band degeneracies fundamentally different from those in Hermitian systems, with exceptional points (EPs)—where eigenvalues and eigenvectors coalesce—standing out as defining singularities that have enabled transformative applications in optics, acoustics, circuits, and so on, from chiral mode switching and enhanced sensing to nonreciprocal transport. In three-dimensional (3D) non-Hermitian systems, such exceptional degeneracies extend into one-dimensional closed exceptional loops (ELs), whose global geometry can exhibit nontrivial knot and link topologies, a feature with no Hermitian analog and untapped potential for topological engineering. Here, we report a universal, constructive framework for realizing arbitrary knotted and linked ELs in 3D minimal two-band non-Hermitian systems, forging the first direct and systematic correspondence between knot theory and non-Hermitian band degeneracies. Leveraging Alexander’s theorem, we start from any knot or link encoded by a braid representation and design tight-binding Hamiltonians whose ELs faithfully replicate the prescribed knot/link topology in momentum space, enabling a rigorous classification of non-Hermitian topological phases via core knot invariants including braid words, Alexander polynomials, and Seifert surfaces. A key fundamental advance is that these knotted ELs are generically stable, requiring no symmetry protection or fine-tuning, and host non-Hermitian metallic phases characterized by Seifert surfaces that encode the defective nature of exceptional degeneracies—an essential distinction from Hermitian nodal lines, which rely on symmetries for their stability. We further demonstrate that knotted ELs can be continuously deformed and untied through deterministic topological transitions driven by a single tunable parameter, which induces controlled reconnection events of EPs and provides an experimentally actionable mechanism for manipulating global knot topology in momentum space. We also propose a concrete experimental realization of knotted and linked ELs in acoustic systems with tunable nonreciprocal couplings, validating the feasibility of observing these topological degeneracies in tabletop experiments. Parallel to the far-reaching impact of EPs across engineered platforms, our results establish knot and link topology as a universal organizing principle for non-Hermitian topological matter and unlock broad applicability for knotted ELs in photonic crystals, acoustic metamaterials, electrical circuits, and cold-atom systems—paving the way for next-generation topology-driven devices with reconfigurable topological modes, robust nonreciprocal responses, and novel spectral engineering capabilities.

I. INTRODUCTION

Exceptional degeneracies represent a defining hallmark of non-Hermitian physics, differing fundamentally from their Hermitian counterparts. At their core are exceptional points (EPs)—defective spectral singularities where eigenvalues and eigenvectors coalesce, rendering the Hamiltonian non-diagonalizable [1–4]. These degeneracies arise generically in open and driven systems and have been experimentally realized across diverse platforms, including photonics [5–10], acoustics [11–13], mechanics [14, 15], electrical circuits [16, 17], and active matter [18, 19]. Acting as branch points on the complex energy Riemann surface, EPs give rise to striking physical effects such as chiral mode switch-

ing [20, 21], mode selection [22], nontrivial spectral winding [23, 24], and enhanced parametric response [17, 25, 26], establishing them as fundamental building blocks of non-Hermitian phenomena.

In momentum space, the dimensionality of exceptional degeneracies is governed by codimension arguments: in two-dimensional (2D) systems, EPs typically appear as isolated point defects [27, 28] or in pairs connected by open Fermi arcs [29, 30], while in three-dimensional (3D) systems, they generically extend into one-dimensional (1D) manifolds termed exceptional lines. These extended non-Hermitian degeneracies exhibit robustness against perturbations, enabling the formation of diverse configurations including closed exceptional rings (ERs) [14, 31], intersecting exceptional chains (ECs) [15, 32], and more elaborate geometries [33]. As embedded curves in 3D momentum space, exceptional lines possess an intrinsic global geometry that demands a topological characterization beyond mere local stability considerations.

A compelling frontier in non-Hermitian band theory in-

* qilin_cai@ustc.edu.cn

† jhjiang3@ustc.edu.cn

volves engineering nontrivial knot and link topologies within exceptional lines [34–40]. Knotted structures are fundamental to topology and pervade diverse physical contexts, from fluid vortices [41], acoustic vortices [42], and optical fields [43–45] to polymers [46], liquid crystals [41], quantum systems [47], particle physics [48], and topological solitons [49]. Embedding knotted structures into band degeneracies opens new avenues for non-Hermitian topological phases of matter, where abstract knot invariants may acquire direct physical significance through measurable spectral and dynamical signatures. Several prior works have demonstrated knotted or linked exceptional loops (ELs) in specific models [34–40], revealing intriguing connections between non-Hermitian topology and exceptional structures.

Despite these advances, a general and constructive principle for realizing ELs with arbitrary knot or link topology has remained elusive. Existing approaches typically rely on model-specific designs, implicit fine-tuning, or specialized functional forms, thereby limiting access to only restricted families of knots or links [34, 50]. The fundamental challenge stems from the constrained nature of exceptional degeneracies: ELs emerge as the intersection of multiple real conditions in momentum space, and engineering these constraints to form a prescribed knotted curve is highly non-trivial. Moreover, in most cases, knot topology is identified only a posteriori, without a direct correspondence between the desired knot structure and Hamiltonian construction. This hinders systematic exploration and controlled comparison across distinct knot types, leaving open the critical question of whether a universal non-Hermitian framework exists to encode, realize, and continuously transform any desired knot or link at the level of band degeneracies.

In this work, we address these challenges by presenting a universal and constructive framework for realizing knotted and linked ELs in 3D non-Hermitian systems. Our approach is built on a minimal two-band non-Hermitian Hamiltonian, where exceptional degeneracies arise from the intersection of two real surfaces defined by the real and imaginary parts of the complex energy. By encoding knot and link information into a pair of scalar functions whose zero-level sets intersect non-trivially, we establish a direct correspondence between knot theory and non-Hermitian band degeneracies. A key conceptual advance is the integration of braid theory and semiholomorphic polynomials into non-Hermitian band construction. Leveraging Alexander’s theorem [51], which states that every knot or link can be represented as the closure of a braid, we develop a systematic pipeline: starting from a braid word, we construct a trigonometric braid, promote it to a braid polynomial, and ultimately derive a semiholomorphic polynomial whose nodal set on the three-sphere realizes the target knot or link. By embedding this construction into Bloch momentum space via a suitable mapping from the Brillouin zone to complex coordinates, we obtain tight-binding lattice models that host ELs with the prescribed knot or link topology.

Beyond static topology, we further demonstrate that knotted ELs can be continuously untied through controlled topological transitions. Tuning a single continuous parameter that governs the effective width of the braid induces determinis-

tic sequences of reconnection events, mediated by the motion, merging, and splitting of exceptional points (EPs). This process provides an experimentally accessible protocol for manipulating knot topology in momentum space, transforming knotted ELs into unlinked or unknotted configurations. Importantly, while the induced pathways are not necessarily minimal in the mathematical sense of the unknotting number, they are continuous, robust, and experimentally feasible—making them particularly well-suited for real-world implementations. More broadly, this work establishes a general bridge between knot theory and non-Hermitian band degeneracies, elevating ELs from geometric features to topological objects classified by knot invariants.

The remainder of this work is organized as follows. In Sec. II, we present the theoretical framework for defective Hamiltonians that host ELs in non-Hermitian systems, establishing the fundamental conditions for exceptional degeneracies. In Sec. III, we develop universal and constructive approach to designing knotted and linked ELs, leveraging braid theory and semiholomorphic polynomials to encode arbitrary knot topology into band structures. We then demonstrate the methodology in Sec. IV through concrete tight-binding models, where we realize and analyze exemplary ELs configurations including torus knots/links (Sec. IV A) such as the Trefoil knot 3_1 and the Hopf link 2_1^2 , lemniscate knots/links (Sec. IV B) such as the Figure-eight knot 4_1 , the knot 6_3 and the Borromean link 6_3^2 , other intricate knot such as the Three-twist knot 5_2 (Sec. IV C) and the Miller-Institute knot 6_2 (Sec. IV D), and complex multi-component links such as the Whitehead link 5_1^2 (Sec. IV E). In Sec. V, We further show that knotted ELs can be continuously untied to unknotted or unlinked configurations by increasing the width of braid. In Sec. VI, we propose a possible experimental scheme for realizing ELs in electro-acoustic systems. In Sec. VII, we conclude this work with several outlooks. Additional mathematical background on Seifert surfaces (Appendix A) and knot invariants (Appendix B) is provided in the Appendices to complement the main text. In Appendix C, we present some of specific form of the Hamiltonians for tight-binding models mentioned in Sec. IV.

II. THE DEFECTIVE HAMILTONIAN APPROACH

An interaction-free two-band system with particle-hole symmetry serves as a minimal yet powerful platform for exploring novel topological phenomena. Its Hamiltonian in momentum space is expressed in the most general form as

$$\hat{H}(\mathbf{k}) = \mathbf{d}(\mathbf{k}) \cdot \boldsymbol{\sigma} = [d_R(\mathbf{k}) + id_I(\mathbf{k})] \cdot \boldsymbol{\sigma}, \quad (1)$$

where $\boldsymbol{\sigma} = (\sigma_x, \sigma_y, \sigma_z)$ are the Pauli matrices, and $d_R(\mathbf{k})$ and $d_I(\mathbf{k})$ are real-valued vector fields governing the Hermitian and non-Hermitian parts of the Hamiltonian, respectively. The corresponding energy eigenvalues are given by $E_{\pm} = \pm\sqrt{\mathbf{d}(\mathbf{k}) \cdot \mathbf{d}(\mathbf{k})}$. The condition for spectral degeneracy, where the two bands coalesce except trivial case $\mathbf{d}(\mathbf{k}) = 0$, is $\mathbf{d}(\mathbf{k}) \cdot \mathbf{d}(\mathbf{k}) = 0$. Decomposing this complex equation

into real and imaginary parts yields two fundamental conditions:

$$\begin{aligned} \text{Re}[E^2] &= \mathbf{d}_R^2(\mathbf{k}) - \mathbf{d}_I^2(\mathbf{k}) = 0, \\ \text{Im}[E^2] &= 2\mathbf{d}_R(\mathbf{k}) \cdot \mathbf{d}_I(\mathbf{k}) = 0. \end{aligned} \quad (2)$$

The solutions to Eqs. (2) and the resulting geometry of the Fermi surface are strongly dependent on the dimensionality of the system. In 2D systems, each condition generally describes a 1D curve in the Brillouin zone. The intersection points of two curves are zero-dimensional (0D) degeneracies known as EPs. At these EPs, the Hamiltonian becomes defective, with coalescing eigenvalues and eigenvectors, leading to a branch point singularity in the complex energy Riemann surface. Generally, EPs in 2D systems appear in pairs and are connected by open Fermi arcs [29, 30].

In 3D systems, the situation becomes more intricate and richer. Here, each condition in Eq. (2) generally defines a 2D manifold. Their intersection, where both requirements are simultaneously satisfied, typically forms a 1D curve. This curve constitutes an exceptional line, a continuous set of EPs. In contrast to the isolated EPs in 2D systems, exceptional lines are robust topological defects in 3D momentum space and can give rise to intricate morphology such as unknotted ERs [31], self-intersected ECs [15, 32] and even knotted [34–36] and linked [37–39] ELs. These ELs configurations are further connected by *Seifert surface* [34]. Mathematically, a Seifert surface is defined as an oriented, connected, and open surface whose boundary coincides with the knot or link itself (see Appendix A).

To illustrate how knotted or linked ELs emerge from the intersection of surfaces satisfying the general degeneracy conditions, we construct a specific model by considering two real continuous functions, $f_1(\mathbf{k})$ and $f_2(\mathbf{k})$, that vanish on two distinct surfaces in momentum space. The real and imaginary parts of the \mathbf{d} -vector are then encoded as

$$\mathbf{d}_R(\mathbf{k}) = [f_1(\mathbf{k}), \Lambda, 0], \quad \mathbf{d}_I(\mathbf{k}) = [0, f_2(\mathbf{k}), \Lambda], \quad (3)$$

where Λ is a non-zero real constant. Substituting Eq. (3) into the general energy-squared formulae Eq. (2) yields the following simplified components

$$\text{Re}[E^2] = f_1^2 - f_2^2, \quad \text{Im}[E^2] = 2f_2\Lambda. \quad (4)$$

This construction provides a direct pathway to design exceptional non-Hermitian degeneracies. The functions f_1 and f_2 can be chosen such that their zero-level sets, $f_1^{-1}(0) \cap f_2^{-1}(0)$, represent surfaces with a topologically nontrivial intersection in the Brillouin zone. The parameter Λ then controls the coupling between the real and imaginary sectors of the Hamiltonian. For sizable Λ , the exceptional knots or links arising from the intersection of the surfaces defined by $\text{Re}[E^2] = 0$ and $\text{Im}[E^2] = 0$ will inherit the knot or link topology of the intersection between the kernels (zero surfaces) of f_1 and f_2 . Since the Hamiltonian exhibits a spectral degeneracy ($E = 0$) while \mathbf{d}_R and \mathbf{d}_I remain finite and non-parallel at these nodes, they are indeed defective lines of the non-Hermitian metals.

III. DESIGN STRATEGY FOR KNOTS AND LINKS

Step 1: Specifying a knot or link. To construct scalar functions f_1 and f_2 such that the intersection of their kernels generates described knots or links \mathcal{K} , a mathematically rigorous method for specifying a knot or link leverages Alexander's theorem [51], which asserts that every knot and link \mathcal{K} can be represented as a closed braid $\bar{\mathcal{B}}_{\mathcal{K}}$. A braid \mathcal{B} of s strands is defined by their trajectories between two parallel planes, with no backward motion in the intervening region. The corresponding knot or link \mathcal{K} is formed by connecting the respective endpoints on the two planes in a one-to-one fashion, an operation known as closure. The topology of the resulting structure is entirely determined by the sequence of crossings between the strands. This sequence is algebraically encoded as a braid word, composed of braiding group generators $\sigma_i^{\pm 1}$, where σ_i denotes the i -th strand crossing over the $(i+1)$ -th strand, and σ_i^{-1} denotes the under-crossing. The braid generators obey two fundamental relations: the commuting relation between non-adjacent strands $\sigma_i\sigma_j = \sigma_j\sigma_i$ for $|i-j| \geq 2$, and the braid relation $\sigma_i\sigma_{i+1}\sigma_i = \sigma_{i+1}\sigma_i\sigma_{i+1}$, which underpins the Yang-Baxter equation [52]. It is crucial to note that due to these relations and Markov moves, the mapping from a braid word to a knot type is many-to-one. Nevertheless, any specific braid word uniquely defines a knot, providing an unambiguous starting point for constructing a Hamiltonian. For instance, the braid word σ_1^2 yields the Hopf link, and σ_1^3 produces the Trefoil knot.

Step 2: Finding a suitable trigonometric braid. The trigonometric representation serves as a foundational step, leveraging simplicity in Fourier components to approximate the knot's structure. A braid \mathcal{B} on s strands is parametrized as

$$B_{\mathcal{K}} = \bigcup_{j=0}^{s-1} (X(t+2\pi j), Y(t+2\pi j), t), \quad t \in [0, 2\pi), \quad (5)$$

where $X(t)$ and $Y(t)$ are carefully designed trigonometric functions. The function $X(t)$ controls the transverse positions of the strands, generating intersections at parameters t_i corresponding to crossings, while $Y(t)$ determines the signs (positive for over-crossings, negative for under-crossings) based on the strand order and knot topology. In general, for any knot or link \mathcal{K} , a trigonometric braid representation can be constructed by first identifying a *minimal braid word* [53] close to \mathcal{K} . The functions $X(t)$ and $Y(t)$ are typically chosen as finite Fourier series, such as $X(t) = \sum_k a_k \cos(\omega_k t + \phi_k)$, $Y(t) = \sum_k b_k \sin(\gamma_k t + \psi_k)$, where the coefficients a_k, b_k , frequencies ω_k, γ_k , and phase ϕ_k and ψ_k are carefully selected to replicate the crossing sequence of the braid word. Our approach emphasizes algebraic simplicity, often minimizing the number of Fourier terms and favoring rational coefficients to facilitate subsequent polynomial mappings. The resulting parametric curve $T_{\mathcal{K}} = \bigcup_{j=0}^{s-1} (X(t+2\pi j), Y(t+2\pi j))$ is periodic with period $2\pi s$ (for s strands) and exhibits symmetries that reflect the knot's structure, providing a robust basis for encoding knots into complex functions.

Step 3: From trigonometric braid to semiholomorphic polynomial. To construct a complex-valued polynomial func-

tion whose nodal set is the desired knot or link \mathcal{K} , we proceed by encoding the trigonometric braid representation into a polynomial map. The construction involves defining a braid polynomial, generalizing it to a semiholomorphic polynomial on \mathbb{C}^2 , and then restricting it to the unit three-sphere \mathcal{S}^3 . First, for a braid on s strands parametrized by trigonometric functions $X(t)$ and $Y(t)$, we define the braid polynomial $\rho_a(u, t)$ as a function of a complex variable u and the braid parameter t ,

$$\rho_a(u, t) = \prod_{j=0}^{s-1} (u - a[X(t + 2\pi j) + iY(t + 2\pi j)]), \quad (6)$$

where $a > 0$ is a scaling parameter that controls the geometric width of the braid trajectory. For sufficiently small a , the braid trajectory lies close to the origin in the u -plane, ensuring that the nodal set on \mathcal{S}^3 is isotopic to the closed braid [54, 55], *i.e.*, the desired knot or link \mathcal{K} . This polynomial is of degree s in u , and its roots trace the positions of the braid strands in the complex u -plane. To close the braid and embed it into a higher-dimensional space, we generalize $\rho_a(u, t)$ to a semi-holomorphic function $F_a(u, v, \bar{v})$ by replacing the dependence on t with the complex variable v . Specifically, we set $t = \arg(v)$ and use de Moivre's theorem to express $\cos(nt) \rightarrow \frac{v^n + \bar{v}^n}{2}$ and $\sin(nt) \rightarrow \frac{v^n - \bar{v}^n}{2i}$. This yields a semi-holomorphic polynomial (holomorphic in u but depending on both v and \bar{v}) which can be written as

$$F_a(u, v, \bar{v}) = \text{polynomial in } u, v, \bar{v}. \quad (7)$$

The function F_a is defined on \mathbb{C}^2 . Of particular interest is the restriction of F_a to the unit three-sphere $\mathcal{S}^3 = \{(u, v) \in \mathbb{C}^2 : |u|^2 + |v|^2 = 1\}$. A key objective is to obtain an explicit form of $F_a : \mathcal{S}^3 \rightarrow \mathbb{C}$ whose preimage of zero $F_a^{-1}(0)$ realized the specific knot \mathcal{K} . The procedure for constructing such a function F_a from a given knot \mathcal{K} is systematic and general, as summarized by the following theorem:

Theorem 1. For every knot or link \mathcal{K} there is a function $F_a : \mathbb{C}^2 \rightarrow \mathbb{C}$ such that $F_a^{-1}(0) \cap \mathcal{S}^3 = \mathcal{K}$ and F_a is a polynomial in complex variables u , v and \bar{v} , *i.e.*, $F_a(u, v, \bar{v})$ is a semiholomorphic polynomial.

In contrast to generalized algorithmic methods [55, 56] that may produce complex parameterizations, our method demonstrates notable benefits for specific braid configurations. Specifically, when applied to short, symmetric braids with a limited number of strands, our method facilitates the derivation of polynomial parameterizations that are remarkably concise, characterized by fewer terms and lower orders. For example, in the case of the knot 5_2 , the parameterization obtained via our method resulted in only two terms for both functions $X(t)$ and $Y(t)$, with a maximum order of five (see the following Sec. IV C). This underscores the capability of our method to yield efficient and simplified representations for amenable braid structures, highlighting its utility in scenarios where parametric simplicity is prioritized.

Step 4: Constructing non-Hermitian Hamiltonian with knotted or linked ELs. To effectively bridge the universal construction of non-Hermitian metals with knotted and

linked ELs with experimentally feasible physical systems, we now demonstrate their realization in tight-binding lattice models. This approach translates abstract topological concepts into tangible Hamiltonians with local hopping terms, enabling implementation in platforms such as photonic crystals [57], acoustic metamaterials [42], or other condensed matter setups [58]. The key challenge lies in mapping from momentum space \mathbb{T}^3 to \mathbb{C}^2 while preserving the intricate knot topology of ELs. Here, we present a general framework for constructing tight-binding models that host knotted ELs, using the formalism outlined in Eqs. (1) and (3). To ensure that f_a encapsulates the braid information, we decompose it into a composition of mappings [59]

$$f_a = F_a \circ G : \mathbb{T}^3 \xrightarrow{G} \mathbb{C}^2 \xrightarrow{F_a} \mathbb{C}, \quad (8)$$

where G is a parametrization mapping from the Brillouin zone \mathbb{T}^3 to \mathbb{C}^2 , designed to preserve Bloch periodicity using trigonometric functions,

$$\begin{aligned} v(\mathbf{k}) &= \sin(k_x) + i\sin(k_y), \\ u(\mathbf{k}) &= P \sum_{\alpha=x,y,z} \cos(k_\alpha) - Q + i\sin(k_z), \end{aligned} \quad (9)$$

where P and Q are real parameters introduced to allow tuning of the EL geometry and topology, ensuring the knotted EL is accurately represented in the tight-binding model. Finally, we express the function as a complex scalar field

$$f_a(\mathbf{k}) = f_1(\mathbf{k}) + if_2(\mathbf{k}), \quad (10)$$

where f_1 and f_2 are real-valued scalar functions we look for. The corresponding tight-binding is then obtained by inserting Eq. (10) into Eq. (3).

IV. EXAMPLES IN TIGHT-BINDING MODELS

We have established a universal theoretical for constructing knotted ELs in above Sec. III and now detailed its application to torus knots/links (Sec. IV A) and lemniscate knots (Sec. IV B). To demonstrate the scope and utility of this constructing beyond these specialized families, we now apply it to a curated sequence of knots and links in continuum models, presented in order of increasing topological complexity.

We begin with torus knots/links (Sec. IV A) such as the Trefoil knot 3_1 and the Hopf Link 2_2^2 , which serve as symmetric benchmarks, followed by lemniscate knots/links (Sec. IV B) such as the Figure-eight knot 4_1 , the knot 6_3 and the Borromean link 6_3^2 , which exhibit hypocycloidal geometries. The sequence then progresses to the Three-twist knot 5_2 (the simplest non-fibered knot, Sec. IV C) and the Miller-Institute knot 6_2 (fibred and hyperbolic knot, Sec. IV D), each exemplifying distinct ELs configurations. Finally, we generalize to multi-component links such as the Whitehead link (Sec. IV E), illustrating the framework's seamless extension to links. The construction for each case follows the same consistent methodological pipeline, from a minimal braid representation and its trigonometric parametrization to the derivation

of the braid polynomial and its final promotion to a semiholomorphic polynomial. Each example thus provides a complete blueprint for generating the corresponding topologically stable exceptional line, collectively validating the universality of the proposed theoretical framework.

A. Torus knots and links

Torus knots and links, denoted as $T(p, q)$, are closed cycles embedded on the surface of a standard torus, where p and q are integers representing the number of longitudinal and meridional winding cycles, respectively. The fundamental distinction between these topological objects is determined by the greatest common divisor $r = \gcd(p, q)$. If $r = 1$, the configuration forms a torus knot, a single, embedded curve, whereas if $r > 1$, the parameters p and q are not coprime, resulting in a torus link, a collection of r mutually interlinked, simpler torus knots $T(p/r, q/r)$. These configurations are uniquely characterized by their fundamental group $[\pi_1(\mathcal{S}^3 \setminus T(p, q)) = \langle x, y \mid x^p = y^q \rangle]$ presentations and exhibit exceptional symmetry. For any coprime integers p and q , the torus knots $T(p, q)$ and $T(q, p)$ are isotopic. Notably, all torus knots and links are algebraic and fibered, meaning their complements in \mathcal{S}^3 admit fibrations by Seifert surfaces (see Appendix A).

According to Alexander's theorem, any torus knot/link $T(p, q)$ can be represented as a closed braid. A standard braid representation for $T(p, q)$ is given by the closure of a braid on p strands with the braid word $(\sigma_1 \sigma_2 \dots \sigma_{p-1})^q$. This braid word describes a sequence where the p strands undergo a full set of adjacent crossings, repeated q times, before being connected to form the closed knot or link. Following the general procedure outlined in Sec. III, we construct a trigonometric parametrization for the braid $B_{T(p, q)}$ associated with the knot/link. For a braid on p strands, the parametrization is

$$B_{T(p, q)} = \bigcup_{j=0}^{p-1} (X_T(qt + 2\pi j), Y_T(qt + 2\pi j), t), t \in [0, 2\pi). \quad (11)$$

For the torus knot/link $T(p, q)$, the functions controlling the transverse positions are elegantly given by

$$X_T(t) = \cos\left(\frac{t}{p}\right), \quad Y_T(t) = \sin\left(\frac{t}{p}\right). \quad (12)$$

This parametrization generates a braid where each strand traces a circular path in the transverse plane, with a phase shift of $2\pi/p$ between adjacent strands. The resulting closed braid $\bar{B}_{T(p, q)}$ is isotopic to the torus knot/link $T(p, q)$.

The next step is to encode this braid into a semiholomorphic polynomial $F^{pq}(u, v, \bar{v})$ whose zero level set on the unit 3-sphere \mathcal{S}^3 recovers the desired knot or link. Here we set $a = 1$ and define the braid polynomial $\rho(u, t)$ for the torus knot braid,

$$\rho(u, t) = \prod_{j=0}^{p-1} \left[u - \left(\cos\left(\frac{qt + 2\pi j}{p}\right) + i \sin\left(\frac{qt + 2\pi j}{p}\right) \right) \right]. \quad (13)$$

The terms inside the product correspond to the p -th roots of a complex exponential, leading to a remarkably simple result. In fact, for torus knots/links, the entire construction yields a polynomial that is holomorphic (indeed independent of \bar{v}), given by

$$F^{pq}(u, v) = u^p - v^q. \quad (14)$$

This polynomial is a fundamental object in singularity theory [60]. To see that its intersection with \mathcal{S}^3 is the torus knot/link $T(p, q)$, one can parameterize $u = R_1 e^{i\phi}$ and $v = R_2 e^{i\theta}$ with $R_{1,2} \in \mathbb{R}^+$. The equation (14) enforces a specific relationship between the phase ϕ and θ , $p\phi - q\theta = 0 \pmod{2\pi}$, effectively tracing the (p, q) -torus knot/link on the torus.

Figure 1 presents a series of characteristic ELs with torus knots and links configurations for different parameter pairs (p, q) , providing direct visual confirmation of our theoretical predictions. When the greatest common divisor is $r = \gcd(p, q) = 1$, the non-Hermitian system exhibits a single torus knotted EL structure. The $T(2, 3)$ configuration in Fig. 1(a) displays a characteristic Trefoil morphology, where the EL forms a closed knot after winding twice longitudinally and three times meridionally around the toroidal geometry of the Brillouin zone. The more complex $T(2, 5)$ structure in Fig. 1(b) demonstrates increased winding complexity. These results are in complete agreement with the classical classification of torus knots in knot theory. Particularly noteworthy is the emergence of torus links when $r > 1$. The $T(2, 2)$ configuration in Fig. 1(f), representing a Hopf link, consists of two mutually linked elementary ELs, while $T(3, 3)$ in Fig. 1(i) and $T(3, 6)$ in Fig. 1(j) showcase structures with more components. The number of link components exactly equals the greatest common divisor r , validating our theoretical prediction that the torus link $T(p, q)$ comprises r mutually interlinked $T(p/r, q/r)$ torus knots.

B. Lemniscate knots and links

Lemniscate knots [50] represent a distinguished family of topological structures that generalize the concept of torus knots through their construction as closures of braids derived from generalized lemniscate curves. They are systematically classified by three integers $L(m, n, l)$, where m is the number of strands, n the number of periods, and l the exponent in the trigonometric parameterization of the braid. This classification establishes a natural hierarchy where the case $l = 1$ is topologically equivalent to the standard torus knot $T(m, n)$, while $l \geq 2$ yields the distinctive hypocycloidal geometry characterizing non-torus lemniscate knots. Their algebraic tractability makes them particularly suitable for modeling complex topological phases in physical systems.

The braid word for lemniscate knots can be directly read off from trigonometric parameterization through a systematic analysis of the strand crossings. The braid representation for

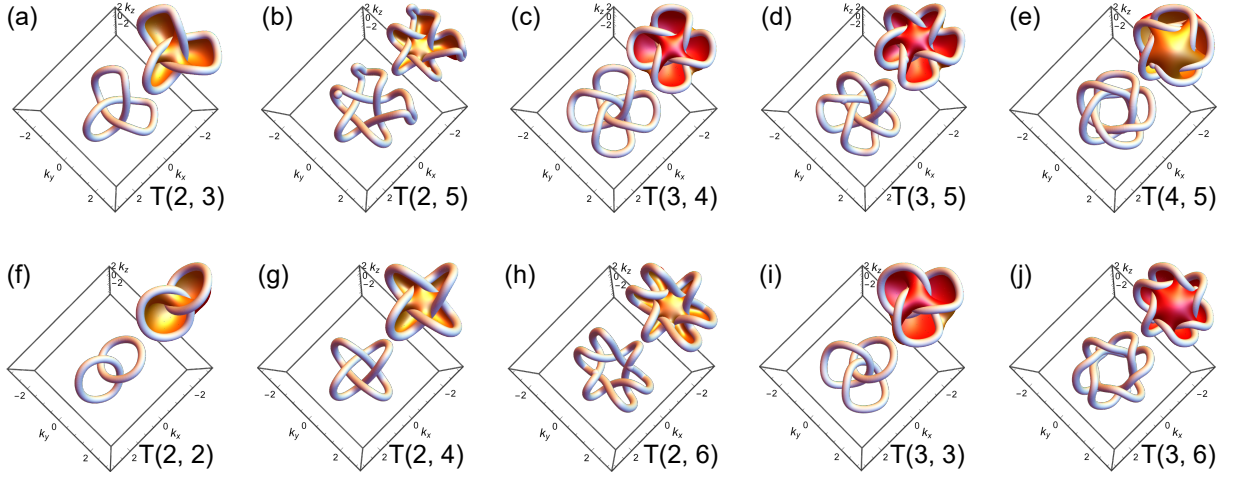


FIG. 1. The exceptional loops (ELs) with torus knots/links $T(p, q)$ configurations (main panels) and their corresponding Seifert surfaces (insets) in tight-binding models. The Seifert surfaces, whose boundaries are knotted and linked ELs, is obtain from the equiphase surface $\arg(f_a) = \pi$. The fundamental distinction between the ELs with torus knots/links configurations is determined by the greatest common divisor $r = \gcd(p, q)$. (a-d) Torus knots if $r = 1$. (e-h) Torus links if $r > 1$. The values of p and q are given at the lower right corner of each panel. $(P, Q) = (1, 2.5)$ is adopted for all panels except panels (e) and (j) with $(P, Q) = (2, 5)$.

lemniscate knots follows the general parameterization

$$B_{L(m,n,l)} = \bigcup_{j=0}^{m-1} (X_L(nt+2\pi j), Y_L(nt+2\pi j), t), t \in [0, 2\pi), \quad (15)$$

with transverse coordinate functions [54]

$$X_L(t) = \cos\left(\frac{t}{m}\right), \quad Y_L(t) = \frac{1}{l} \sin\left(\frac{lt}{m}\right). \quad (16)$$

The braid word is read off by analyzing the strand crossings in the (t, X) -plane projection. Crossings occur at parameter values t_c where the X -coordinates of two distinct strands coincide, *i.e.*, $X_L(nt_c + 2\pi j) = X_L(nt_c + 2\pi k)$ for $j \neq k$. The sign of each crossing (over or under) is determined by comparing the corresponding Y -coordinates at t_c : if $Y_L(nt_c + 2\pi j) > Y_L(nt_c + 2\pi k)$, stand j crosses over strand k , corresponding to a positive generator σ_i ; otherwise, it corresponds to σ_i^{-1} . For the Figure-eight knot $4_1[L(3, 2, 2)]$, the resulting braid word is $(\sigma_1\sigma_2^{-1})^2$, which represents a three-strand braid. As shown in Fig. 2(a1), the strands are labeled 1 (green), 2 (red), and 3 (blue) at $t = 0$, and the corresponding crossings and their signs determined by the Y -coordinate ordering at each t_c are indicated in Fig. 2(b1). The trigonometric braid in Fig. 2(c1) visualizes the full trajectory, highlighting the underlying hypocycloidal geometry. Similarly, the braid word for the knot $6_3[L(5, 2, 2)]$ is read off $(\sigma_1\sigma_3^{-1}\sigma_2\sigma_4^{-1})^2$ but involving five strands [see Figs. 2(a2-c2)].

The parameter l plays a crucial role in modulating the crossing sequence. For $l = 1$, the functions $X_L(t)$ and $Y_L(t)$ describe perfect circles, and the braid word reduces to the regular pattern $(\sigma_1\sigma_2 \dots \sigma_{m-1})^n$, which is the standard braid word for the torus knot $T(m, n)$. For $l \geq 2$, the factor $1/l$ in $Y_L(t)$ compresses the sinusoidal motion in the Y -direction, leading to a higher density of crossings and a more complex sequence

of over- and under-crossings. The crossings associated with odd-indexed generators (*e.g.*, $\sigma_1, \sigma_3, \dots$) typically occur at parameter values $t_c = 2k\pi/m$ for $k = 0, 1, \dots, m-1$, while the crossings for even-indexed generators (*e.g.*, $\sigma_2, \sigma_4, \dots$) occur at $t_c = (2k+1)\pi/m$. The resulting braid word becomes $\mathcal{B}_{L(m,n,l)} = (\sigma_1^{\epsilon_1} \sigma_3^{\epsilon_3} \dots \sigma_2^{\epsilon_2} \sigma_4^{\epsilon_4} \dots)^n$, where the exponents $\epsilon_i \in \{+1, -1\}$ are determined by the relative Y -coordinates at the crossing points. The sequence of ϵ_i may exhibit periodic patterns or symmetries reflecting the hypocycloidal nature of the lemniscate curve. For example, when $l = 2$, the braid word often exhibits an alternating pattern of signs, while for larger l the pattern can become more intricate, involving longer cycles of over- and under-crossings. It provides a direct link between the geometric description of the braid and its algebraic representation in the braid group. The braid word then serves as the foundation for constructing the polynomial function whose zero level set yields ELs with the lemniscate knot in momentum space.

Applying the general procedure outlined in Sec. III, we construct specific semiholomorphic polynomials for two lemniscate knots. For the Figure-eight knot $[4_1]$ in the Rolfsen's table, $L(3, 2, 2]$, the braid word is $(\sigma_1\sigma_2^{-1})^2$ [see Fig. 2(a1)], and the corresponding semiholomorphic polynomial is derived as

$$F_a(u, v, \bar{v}) = 64u^3 - 12a^2u[3 + 2(v^2 - \bar{v}^2)] - a^3[14(v^2 + \bar{v}^2) + (v^4 - \bar{v}^4)]. \quad (17)$$

Similarly, for the knot $6_3[L(5, 2, 2)]$, which involves a 5-strand braid with braid word $(\sigma_1\sigma_3^{-1}\sigma_2\sigma_4^{-1})^2$ [see Fig. 2(a2)], the polynomial is given by

$$F_a(u, v, \bar{v}) = 1024u^5 - 960a^2u^3 - 160a^3u^2(v^2 + \bar{v}^2) + 20a^4u[21 - 10(v^2 - \bar{v}^2)] - a^5[82(v^2 + \bar{v}^2) + (v^4 - \bar{v}^4)]. \quad (18)$$

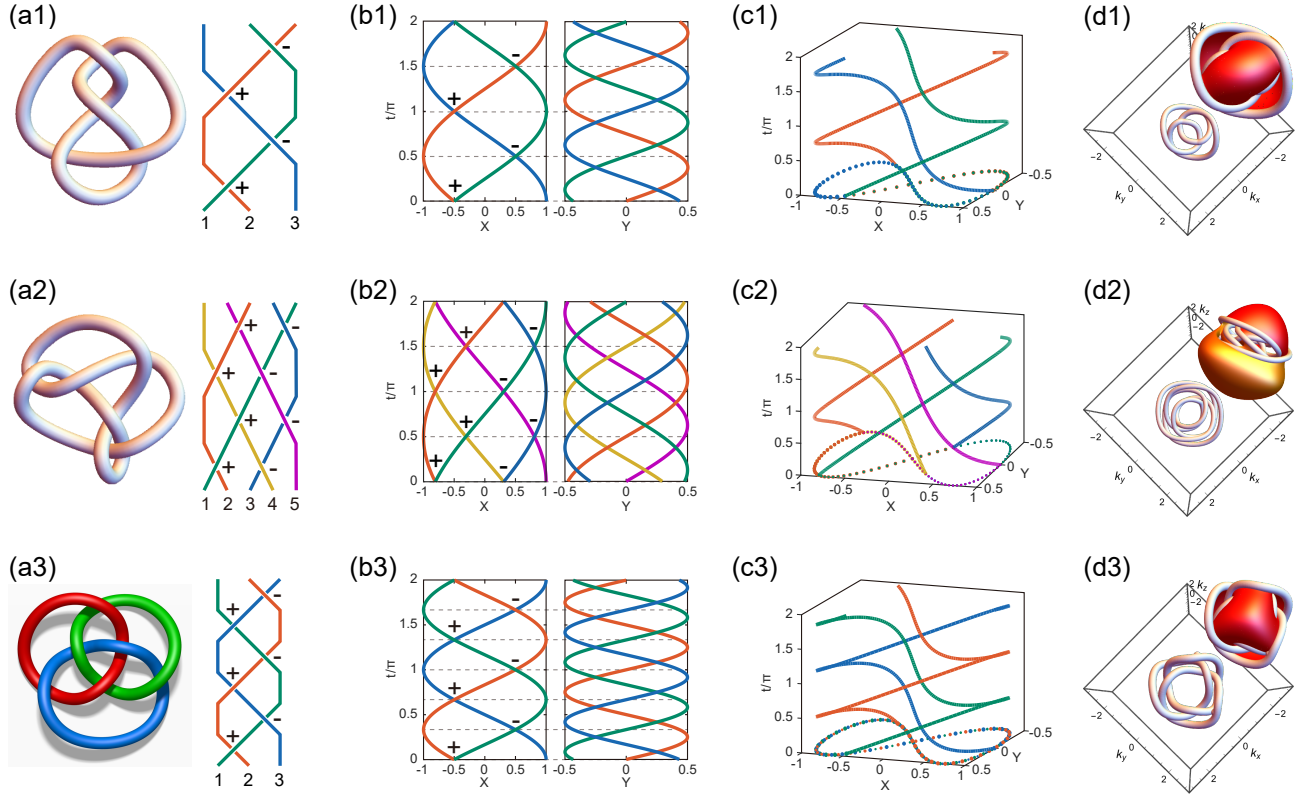


FIG. 2. Constructing exceptional loops (ELs) with lemniscate knots/links configurations in tight-binding model, such as the knotted Figure-eight EL [$T(3, 2, 2)$ in the first row], the knotted 6_3 EL [$T(5, 2, 2)$ in the second row] and linked Borromean ELs [$T(3, 3, 2)$ in the last row]. (a1) Schematic diagram of the Figure-eight knot (left) and its braid word $(\sigma_1\sigma_2^{-1})^2$ (right), which encodes the sequence of crossings for a 3-strand braid. The Figure-eight knot 4_1 is the simplest non-torus knot. Strands are labeled increasing order at $t = 0$: 1(green), 2(red), 3(blue). (a2) Schematic diagram of the 6_3 knot (left) and its braid word $(\sigma_1\sigma_3^{-1}\sigma_2\sigma_4^{-1})^2$ (right), which encodes the sequence of crossings for a 5-strand braid. Strands are labeled increasing order at $t = 0$: 1(green), 2(red), 3(blue), 4(orange), 5(magenta). (a3) Schematic diagram of the Borromean link (left) and its braid word $(\sigma_1\sigma_2^{-1})^3$ (right), which encodes the sequence of crossings for a 3-strand braid. Strands are labeled increasing order at $t = 0$: 1(green), 2(red), 3(blue). (b1-b3) Plot of $X(nt + 2\pi j)$ and $Y(nt + 2\pi j)$ with $j = 0, 1, \dots, m - 1$ from Eq. (16), giving the same unsigned braiding diagram as panels (a1-a3) for $t \in [0, 2\pi]$. The signs “+(-)” in the crossings indicate over(under)-crossing of the adjacent two strands. (c1-c3) Trigonometric braid of the knots/links (solid lines) and their projection on XY -plane (dotted lines) obtained from Eqs. (15-16). (d1-d3) The knotted 4_1 , knotted 6_3 and linked Borromean ELs obtain from Eqs. (17) with $(a, P, Q) = (1, 2, 5)$, Eq. (18) with $(a, P, Q) = (1, 2, 4.6)$ and Eq. (19) with $(a, P, Q) = (1, 2, 4)$, respectively. Inset: The Seifert surface, whose boundaries coincide with the ELs, are obtained from the equiphase surfaces $\arg(f_a) = \pi$.

Lemniscate links are defined using pairs of positive integers m and n that are not coprime. As an example, the Borromean link, denoted as $L(3, 3, 2)$, can be represented via a 3-strand braid with braid word $(\sigma_1\sigma_2^{-1})^3$ [see Fig. 2(a3)]. The corresponding polynomial is given by

$$F_a(u, v, \bar{v}) = 64u^3 - 12a^2u[3 + 2(v^3 - \bar{v}^3)] - a^3[14(v^3 + \bar{v}^3) + (v^6 - \bar{v}^6)]. \quad (19)$$

The zero level set of each Eqs. (17-19) defines a complex scalar field whose EL in momentum space realize the corresponding knotted or linked topology. As illustrated in Figs. 2(d1-d3), the resulting ELs indeed form the Figure-eight knot 4_1 , the 6_3 knot and the Borromean link structure, confirming the validity of the algebraic construction. The insets in Figs. 2(d1-d3) display the associated Seifert surfaces that originate from the non-Hermitian degeneracies, corroborating

the metallic nature of the system.

C. Three-twist knot 5_2

The Three-twist knot (5_2 in the Rolfsen's table) is distinguished as the simplest non-fibred knot. Among all knots with five or fewer crossings, it is the first and thus the most elementary example whose complement $\mathcal{S}^3 \setminus \mathcal{K}$ does not admit the structure of a surface bundle over the circle S^1 . This fibred property, possessed by knots like the torus knots mean the knot complement can be built by suspending a homeomorphism of a Seifert surface. The absence of this structure for 5_2 is detected algebraically by its Alexander polynomial, $\Delta(t) = 2t^2 - 3t + 2$, which fails to be monic, a necessary condition for fibred knots (see Appendix B).

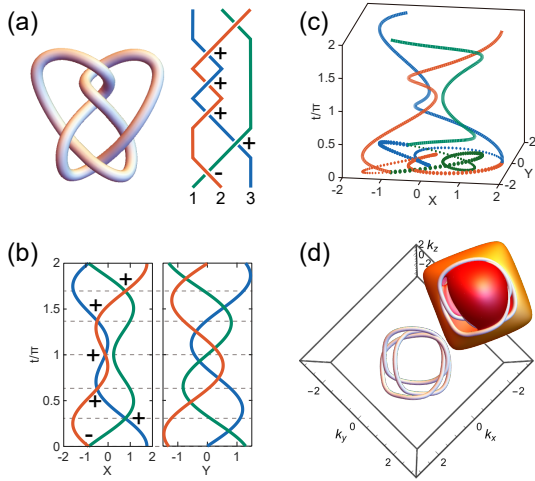


FIG. 3. Constructing the knotted 5_2 exceptional loop (EL) in tight-binding model. (a) Schematic diagram of the knot 5_2 (left) and its braid word $\sigma_1^{-1}\sigma_2\sigma_1^3\sigma_2$ (right), which encodes the sequence of crossings for a 3-strand braid. The Three-twist knot 5_2 is the simplest non-fibred knot. Strands are labeled increasing order at $t = 0$: 1(green), 2(red), 3(blue). (b) Plot of $X(t + 2\pi j)$ and $Y(t + 2\pi j)$ with $j = 1, 2, 3$ from Eq. (21), giving the same unsigned braiding diagram as panel (a) for $t \in [0, 2\pi]$. The signs “+(-)” in the crossings indicate over(under)-crossing of the adjacent two strands. (c) Trigonometric braid of the knot 5_2 (solid lines) and its projection on XY -plane (dotted lines) obtained from Eqs. (20-21). (d) The knotted 5_2 EL obtained from Eq. (23) with $(a, P, Q) = (1/4, 1, 2.1)$. Inset: The Seifert surface, whose boundary coincides with the knotted 5_2 EL, is obtained from the equiphase surface $\arg(f_a) = \pi$.

The construction of Three-twist knotted 5_2 EL begins with its braid representation. The minimal braid word for knot 5_2 is $\sigma_1^{-1}\sigma_2\sigma_1^3\sigma_2$, which encodes the full sequence of crossings for a 3-strand braid. In Figs. 3(a-b), the three strands are distinguished by green, red, and blue color in order at $t = 0$, where the signs “+(-)” in the crossings indicate over(under)-crossings. To geometrically represent this braid, we use a trigonometric parametrization

$$B_{5_2} = \bigcup_{j=0}^2 (X(t + 2\pi j), Y(t + 2\pi j), t), t \in [0, 2\pi], \quad (20)$$

where the transverse coordinate function $X(t)$ is carefully designed to replicate the crossing sequence specified by the braid word as shown in Fig. 3(b), and $Y(t)$ ensures the correct order of over- and under-crossings through periodic behavior [54],

$$\begin{aligned} X(t) &= \cos\left(\frac{2t}{3}\right) + \frac{3}{4}\cos\left(\frac{5t}{3}\right), \\ Y(t) &= \sin\left(\frac{4t}{3}\right) + \frac{1}{2}\sin\left(\frac{t}{3}\right). \end{aligned} \quad (21)$$

The choice of these trigonometric terms is not unique, but optimized to minimize complexity while preserving the knot topology, with coefficients selected to match the braid word’s crossing signs. The trigonometric braid defined by Eqs. (20-21) whose projection onto the XY -plane visually confirms the intended crossing pattern, as shown in Fig. 3(c).

The next step involves encoding geometric braid into an algebraic form via a braid polynomial $\rho_a(u, t)$, which serves as an intermediate function before deriving the semiholomorphic polynomial. The braiding polynomial for knot 5_2 defined as

$$\begin{aligned} \rho_a(u, t) &= \prod_{j=0}^2 (u - a[X(t + 2\pi j) + iY(t + 2\pi j)]) \\ &= 256u^3 - 12a^2u\{5 + 8\cos(t) + 4i[4\sin(t) \\ &\quad + 11\sin(2t) + 6\sin(3t)]\} + a^3\{192 \\ &\quad + 372\cos(t) + 256\cos(2t) + 144\cos(3t) \\ &\quad + 108\cos(4t) + 27\cos(5t) - 2i[188\sin(t) \\ &\quad + 102\sin(2t) - 21\sin(3t) - 32\sin(4t)]\}, \end{aligned} \quad (22)$$

where $a > 0$ is a scaling parameter that controls the width of the braid trajectory. The expansion results from multiplying the factors and simplifying the trigonometric expressions, ensuring the roots trace the braid strands in the complex plane. To transition to a polynomial defined on momentum space, we generalize $\rho_a(u, t)$ to a semiholomorphic polynomial $F_a(u, v, \bar{v})$ by replacing the parameter t with complex variables $\arg(v)$. Using the mappings $\cos(nt) \rightarrow \frac{v^n + \bar{v}^n}{2}$ and $\sin(nt) \rightarrow \frac{v^n - \bar{v}^n}{2i}$, we substitute into the expression for Eq. (22) yielding

$$\begin{aligned} F_a(u, v, \bar{v}) &= 512u^3 + 24a^2u(12v^3 - 12\bar{v}^3 + 22v^2 - \\ &\quad 22\bar{v}^2 + 4v - 12\bar{v} - 5) + a^3(384 + \\ &\quad 27v^5 + 27\bar{v}^5 + 44v^4 + 172\bar{v}^4 + 102v^3 + \\ &\quad 186\bar{v}^3 + 460v^2 + 52\bar{v}^2 + 748v - 4\bar{v}). \end{aligned} \quad (23)$$

Finally, the semiholomorphic polynomial Eq. (23) is implemented within the prescribed tight-binding model framework via the composite mapping f_a in Eq. (8). Setting the parameters to $(a, P, Q) = (1/4, 1, 2.1)$ yields the Three-twist knotted 5_2 EL shown in Fig. 3(d). The boundary of equiphase surface, defined by $\arg(f_a) = \pi$ forming a Seifert surface as illustrated in the inset of Fig. 3(d), coincides with the knotted 5_2 EL.

D. Miller-Institute knot 6_2

The Miller-Institute knot (6_2 in the Rolfsen’s table) stands in direct contrast to 5_2 as fibred and hyperbolic knot. As a fibred knot, its complement in S^3 admits a fibration over the circle with a punctured surface of genus two as its fibre, a property immediately detected by its monic Alexander polynomial, $\Delta(t) = 1 - t + 2t^2 - t^3 + t^4$ (see Appendix B).

The construction of the knotted 6_2 EL follows a procedure analogous to that of the knot 5_2 . The minimal braiding word for knot 6_2 is $\sigma_1\sigma_2^{-1}\sigma_1^3\sigma_2^{-1}$. Notably, it shares the same unsigned braid word as knot 5_2 ($\sigma_1^{-1}\sigma_2\sigma_1^3\sigma_2$), meaning the sequences of crossing locations are identical. However, the signs (over/under assignments) of the crossings differ between the two knots, leading to distinct knot types. Therefore, we reuse the same $X(t)$ function to replicate the shared crossing sequence, but must design a new $Y(t)$ function to generate

the specific sign pattern encoded in the 6_2 braid word. We employ the trigonometric parametrization

$$B_{6_2} = \bigcup_{j=0}^2 (X(t+2\pi j), Y(t+2\pi j), t), \quad t \in [0, 2\pi), \quad (24)$$

where

$$X(t) = \cos\left(\frac{2t}{3}\right) + \frac{3}{4}\cos\left(\frac{5t}{3}\right), \quad Y(t) = -\sin\left(\frac{7t}{3}\right). \quad (25)$$

Here, the $X(t)$ function is identical to that used for 5_2 , responsible for creating the correct sequence of crossings. The $Y(t)$ function is chosen as single Fourier component, its specific form ensures the relative heights of the strands at the crossing points yield the precise pattern of over- and under-crossings specified by the 6_2 braid word, as shown in Figs. 4(b-c).

The next step involves encoding geometric braid into an algebraic form via a braid polynomial $\rho_a(u, t)$. The corresponding braid polynomial for knot 6_2 is defined as

$$\begin{aligned} \rho_a(u, t) &= \prod_{j=0}^2 (u - a[X(t+2\pi j) + iY(t+2\pi j)]) \\ &= 256u^3 - 12a^2u\{3[3 + 8\cos(t)] - \\ &\quad 8i[4\sin(3t) + 3\sin(4t)]\} - a^3\{[64\cos(2t) \\ &\quad + 288\cos(3t) + 300\cos(4t) + 27\cos(5t)] \\ &\quad - 4i[21\sin(t) + 16\sin(7t)]\} \end{aligned} \quad (26)$$

where $a > 0$ is a scaling parameter that controls the width of the braid trajectory. The expansion results from multiplying the factors and simplifying the trigonometric expressions, ensuring the roots trace the braid strands in the complex plane. To transition to a polynomial defined on momentum space, we generalize $\rho_a(u, t)$ to a semiholomorphic polynomial $F_a(u, v, \bar{v})$ by replacing the parameter t with complex variables $\arg(v)$. Using the mappings $\cos(nt) \rightarrow \frac{v^n + \bar{v}^n}{2}$ and $\sin(nt) \rightarrow \frac{v^n - \bar{v}^n}{2i}$, we substitute into the expression for Eq. (26) yielding

$$\begin{aligned} F_a(u, v, \bar{v}) &= 512u^3 - 24a^2u(9 + 12v + 12\bar{v} - 16v^3 \\ &\quad + 16\bar{v}^3 - 12v^4 + 12\bar{v}^4) - a^3(-82v \\ &\quad + 82\bar{v} + 64v^2 + 64\bar{v}^2 + 288v^3 \\ &\quad + 288\bar{v}^3 + 300v^4 + 300\bar{v}^4 + 27v^5 \\ &\quad + 27\bar{v}^5 - 64v^7 + 64\bar{v}^7). \end{aligned} \quad (27)$$

Finally, the semiholomorphic polynomial Eq. (27) is implemented within the prescribed tight-binding model framework via the composite mapping f_a in Eq. (8). Setting the parameters to $(a, P, Q) = (1/4, 1, 2.1)$ yields the knotted 6_2 EL shown in Fig. 4(d). The boundary of equiphase surface, defined by $\arg(f_a) = \pi$ forming a Seifert surface as illustrated in the inset of Fig. 4(d), coincides with the knotted 6_2 EL.

E. Whitehead link 5_1^2

The Whitehead link ($L5a1$ in the Thistlethwaite's table, 5_1^2 in the Rolfsen's table of links) is a two-component, five-

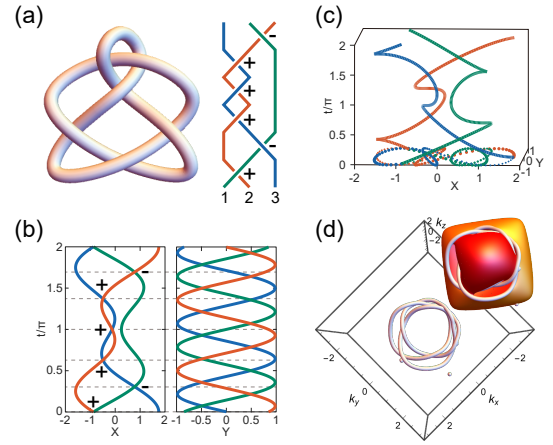


FIG. 4. Constructing the knotted 6_2 exceptional loop (EL) in tight-binding model. (a) Schematic diagram of the knot 6_2 (left) and its braid word $\sigma_1\sigma_2^{-1}\sigma_1^3\sigma_2^{-1}$ (right), which encodes the sequence of crossings for a 3-strand braid. The Miller-Institute knot 6_2 is a fibred and hyperbolic knot. Strands are labeled increasing order at $t = 0$: 1(green), 2(red), 3(blue). (b) Plot of $X(t+2\pi j)$ and $Y(t+2\pi j)$ with $j = 1, 2, 3$ from Eq. (25), giving the same unsigned braiding diagram as panel (a) for $t \in [0, 2\pi]$. The signs “+(-)” in the crossings indicate over(under)-crossing of the adjacent two strands. (c) Trigonometric braid of the knot 6_2 (solid lines) and its projection on XY -plane (dotted lines) obtained from Eqs. (24-25). (d) The knotted 6_2 EL obtained from Eq. (27) with $(a, P, Q) = (1/4, 1, 2.1)$. Inset: The Seifert surface, whose boundary coincides with the knotted 6_2 EL, is obtained from the equiphase surface $\arg(f_a) = \pi$.

crossing link whose deceptive entanglement belies a profound property: while the components are non-trivially linked, removing either one leaves behind a single unknotted circle.

The construction of links follows precisely the same methodological framework established for knots. The key distinction is that a link comprises multiple components, each of which corresponds to a specific subset of strands in its braid representation. For the Whitehead link, its minimal braid has three strands and five crossings, with the braid word $\sigma_1\sigma_2^{-1}\sigma_1\sigma_2^{-1}\sigma_1$. In this representation, strands 2 and 3 together form one component of the link, which traces a simple loop. The remaining strand (strand 1) constitutes the second component, weaving around the first in a lemniscate-like trajectory [see Fig. 5(c)]. This braid structure is captured by the following trigonometric parametrization, where the two components are naturally distinguished by their periods

$$\begin{aligned} B_{L51a} &= (X_2(t), Y_2(t), t) \bigcup_{j=0}^1 (X_1(t+2\pi j), \\ &\quad Y_1(t+2\pi j), t), \quad t \in [0, 2\pi) \end{aligned} \quad (28)$$

The coordinate functions are

$$\begin{aligned} X_1(t) &= \frac{1}{2}\cos\left(\frac{3}{2}t\right) - \cos\left(\frac{1}{2}t\right), \quad Y_1(t) = -\frac{1}{4}\sin\left(\frac{1}{2}t\right); \\ X_2(t) &= -\cos(t), \quad Y_2(t) = -\frac{1}{2}\sin(2t). \end{aligned} \quad (29)$$

Here, the parametrization reflects the braid composition. The first component (strands 2 and 3 of the braid) is defined by $(X_1(t), Y_1(t))$ and completes its path over a 4π interval in t , represented by the union over $j = 0, 1$. The second component (strand 1) is given by $(X_2(t), Y_2(t))$ and has the standard 2π period. The interplay of two trajectories with different periods generates the characteristic five-crossing topology of the Whitehead link.

The subsequent algebraic encoding proceeds identically to the knot case. The braid polynomial $\rho_a(u, t)$ is constructed as the product whose roots trace parametrized strands

$$\begin{aligned} \rho_a(u, t) &= (u - a[X_2(t) + iY_2(t)]) \times \\ &\prod_{j=0}^1 (u - a[X_1(t + 2\pi j) + iY_1(t + 2\pi j)]) \\ &= 128u^3 + 64au^2[2\cos(t) + i\sin(2t)] + 4a^2u \\ &\quad \{[-19 - \cos(t) + 16\cos(2t) - 4\cos(3t)] \\ &\quad + 4i[-3\sin(t) + \sin(2t)]\} - a^3\{2[3 \\ &\quad + 16\cos(t) + 5\cos(2t) - 10\cos(3t) \\ &\quad + 2\cos(4t)] + i[-11\sin(t) + 62\sin(2t) \\ &\quad - 7\sin(3t) - 16\sin(4t) + 4\sin(5t)]\}. \end{aligned} \quad (30)$$

Finally, applying the substitution rules $\cos(nt) \rightarrow \frac{v^n + \bar{v}^n}{2}$ and $\sin(nt) \rightarrow \frac{v^n - \bar{v}^n}{2i}$ yields the corresponding semiholomorphic polynomial

$$\begin{aligned} F_a(u, v, \bar{v}) &= 256u^3 + 64au^2(2v + 2\bar{v} + v^2 - \bar{v}^2) \\ &\quad + 4a^2u(-38 - 13v + 11\bar{v} + 20v^2 \\ &\quad + 12\bar{v}^2 - 4v^3 - 4\bar{v}^3) - a^3(12 + 21v \\ &\quad + 43\bar{v} + 72v^2 - 52\bar{v}^2 - 27v^3 - 13\bar{v}^3 \\ &\quad - 12v^4 + 20\bar{v}^4 + 4v^5 - 4\bar{v}^5). \end{aligned} \quad (31)$$

Finally, the polynomial Eq. (31) is implemented within the prescribed tight-binding model framework via the composite mapping f_a in Eq. (8). Setting the parameters to $(a, P, Q) = (1/4, 2, 4)$ yields the two-component EL corresponding to the Whitehead link configuration shown in Fig. 5(d). The boundary of equiphase surface, defined by $\arg(f_a) = \pi$ forming a Seifert surface as illustrated in the inset of Fig. 5(d), coincides with the Whitehead linked EL.

Figures 1-5 collectively demonstrate the effectiveness of our construction method. The topology of the resulting ELs agrees precisely with the desired knot types, while the associated Seifert surfaces explicitly confirm the metallic behavior originating from non-Hermitian degeneracies. By integrating algebraic braid theory with semiholomorphic polynomial functions, this approach provides a versatile and systematic framework for designing and realizing novel non-Hermitian topological phases of matter in experimental platforms such as photonic crystals and acoustic metamaterials.

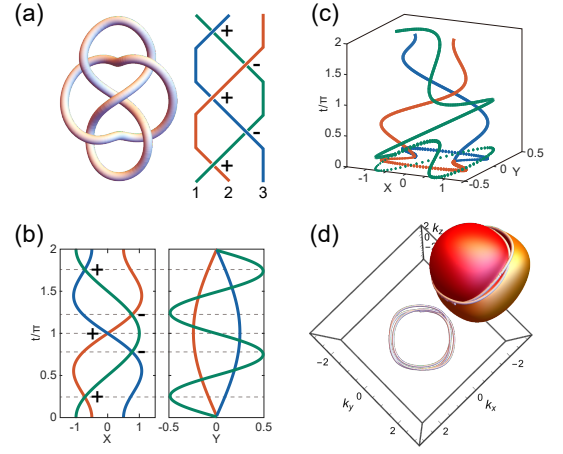


FIG. 5. Constructing the linked Whitehead exceptional loops (ELs) in tight-binding model. (a) Schematic diagram of the Whitehead link (left) and its braid word $\sigma_1\sigma_2^{-1}\sigma_1\sigma_2^{-1}\sigma_1$ (right), which encodes the sequence of crossings for a 3-strand braid. Strands are labeled in increasing order at $t = 0$: 1(green), 2(red), 3(blue). (b) Plot of $X_1(t)$, $X_1(t + 2\pi)$, $X_2(t)$ and $Y_1(t)$, $Y_1(t + 2\pi)$, $Y_2(t)$ from Eq. (29), giving the same unsigned braiding diagram as panel (a) for $t \in [0, 2\pi]$. The signs “+(-)” in the crossings indicate over(under)-crossing of the adjacent two strands. (c) Trigonometric braid of the Whitehead link (solid lines) and its projection on XY -plane (dotted lines) obtained from Eqs. (28-29). (d) The linked Whitehead ELs obtained from Eq. (31) with $(a, P, Q) = (1/4, 2, 4)$. Inset: The Seifert surface, whose boundary coincides with the linked Whitehead ELs, is obtained from the equiphase surface $\arg(f_a) = \pi$.

V. TOPOLOGICAL TRANSITIONS: UNTIE KNOTTED ELS

The problem of untying a knot, transforming it into an unknot or a set of unknots through a finite sequence of local moves, is a fundamental question in knot theory. Mathematicians quantify this complexity through invariants like the *unknotting number* [52], defined as the minimum number of crossing changes required to convert a knot into the unknot. Considerable progress has been made in bounding or computing the unknotting number for specific knot families, often through deep results in gauge theory [61], Heegaard Floer homology [62], or combinatorial methods [63]. Seminal works by Kronheimer and Mrowka [64], and later by Lackenby [63], have established important constraints and achieved precise calculations for many knots. However, determining the unknotting number in general is computationally challenging; related decision problems, such as determining the genus of a knot from its diagram, are known to be NP-hard, highlighting the intrinsic complexity of finding an optimal unknotting pathway.

In our Non-Hermitian systems, we implement a controlled unknotting via a single, continuously tunable parameter a . The process is analogous to performing a specific, algorithmically defined sequence of reconnections (physically realized as exceptional chain formations and splittings) on the knotted EL. While the pathway induced by increasing a may not cor-

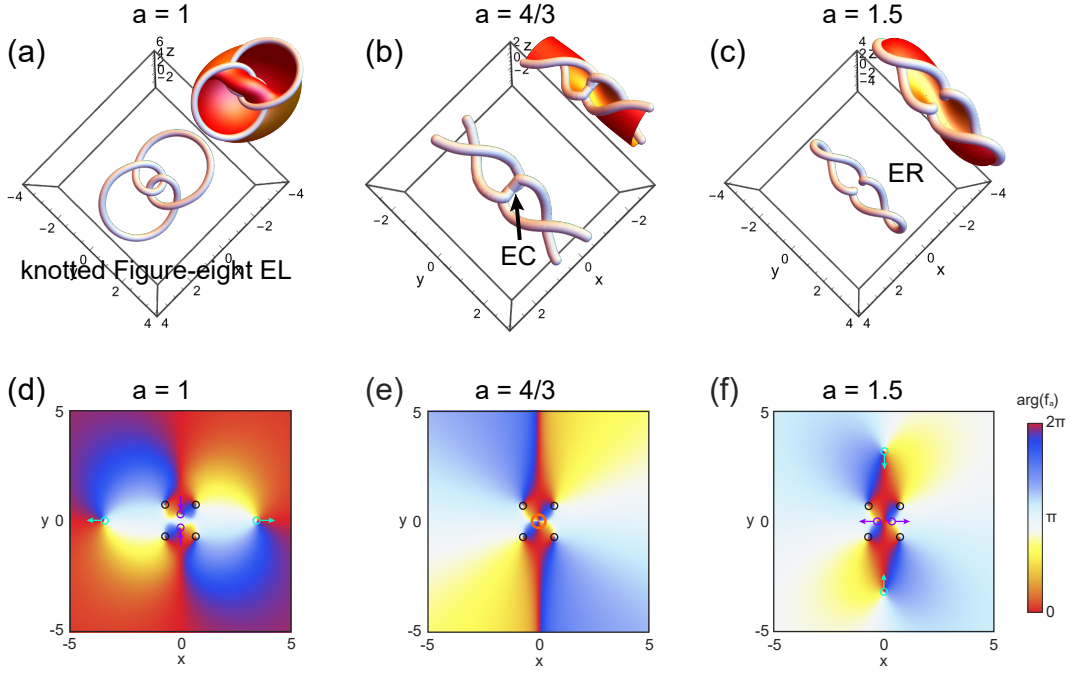


FIG. 6. The exceptional loops (ELs) obtained from Eq. (17) and their evolutions by continuously increasing scaling parameter a . (a-c) Evolution of the morphology of ELs (main panels) and their Seifert surfaces (insets) by continuously increasing the scaling parameter a , starting from the knotted 4_1 EL with $a = 1$ in Fig. 6(a). The ELs configurations are labeled according to the context of the main text. (d-f) Color scale: $\arg(f_a)$ in xy -plane. Circles: vortices in $\arg(f_a)$ by using standard stereographic mapping Eq. (32), which correspondence to exceptional points (EPs). The arrows indicate the moving of EPs. The value of scaling parameter a is given in the top of each panel.

respond to the mathematically minimal unknotting number, it provides a universal and experimentally accessible algorithm for systematically simplifying knot topology. In the following, we demonstrate this principle through the deliberate untying of two distinct knots: the Figure-eight knot 4_1 (Sec. VA) and the Three-twist knot 5_2 (Sec. VB).

The function F_a is defined on \mathbb{C}^2 , but we are interested in its restriction to the unit three-sphere $\mathcal{S}^3 = \{(u, v) \in \mathbb{C}^2 : |u|^2 + |v|^2 = 1\}$. For a better visualization of the knotted ELs configurations, in the following analysis, we will adopt the standard stereographic coordinates to map \mathcal{S}^3 to 3D Euclidean space \mathbb{R}^3

$$u = \frac{x^2 + y^2 + z^2 - 1 + 2iz}{x^2 + y^2 + z^2 + 1}, v = \frac{2(x + iy)}{x^2 + y^2 + z^2 + 1}. \quad (32)$$

A. Untie Figure-eight knotted 4_1 EL configuration

The first case is to untie EL with the Figure-eight knot 4_1 configuration. The initial EL configuration at $a = 1$ obtained from Eq. (17), shown in Fig. 6(a), consists of a single, closed, and self-crossing loop forming a Figure-eight knot, fully contained within a compact region of the Brillouin zone. Upon increasing the parameter to the critical value $a = 4/3$ [Fig. 6(b)], a significant reconfiguration occurs. The inner segments of the knot, which locally resemble hyperbolic branches, meet together at the Γ point (the origin of the Brillouin zone).

At the critical point, they connect at the origin, forming a distinctive, flat ribbon-like structure identified as a EC. Simultaneously, the outer loops of the original knot break, transforming into open exceptional arcs that extend outward.

A further increase to $a = 3/2$, corresponding to Fig. 6(c), completes the unknotting process through a second reconnection. The central EC splits apart, resolving the previous entanglement of the inner branches. Simultaneously, the open exceptional arcs from the previous stage reconnect with each other, contracting and merging to form a single, 3D coiled unknotted ER.

The topological transitions and morphological evolution of ELs described above are directly linked to the underlying movements and reconnection of the associated EPs, as revealed by the phase of the function f_a in the xy -plane, shown in Figs. 6(d-f). The vortices in $\arg(f_a)$, marked by circles, correspond to the EPs whose trajectories trace ELs in 3D momentum space. Around Γ point, four EPs (marked as black circles) remain stationary. However, two other pairs of EPs, indicated by green and purple circles, exhibit distinct motions as a increases, as indicated by arrows. Firstly, the purple EPs are moving slowly towards Γ point along the y -axis, while the green EPs are moving rapidly away from Γ point along the x -axis. As a increases to $4/3$ [Fig. 6(e)], the vortices move (as indicated by purple arrows) and reconfigure, with pairs meeting at the Γ point, coinciding with the formation of the central EC in Fig. 6(b). Simultaneously, the vanishment of purple EPs pair at infinite coincides with the breaking of the knot.

Subsequently, as a further increases to $3/2$, the subsequent rearrangement and separation of these EP pairs facilitate the splitting of the TEC and the reconnection of the open exceptional arcs into the final unknotted ER in Fig. 6(a). More slice diagrams of $\arg(f_a)$ in xy -plane, can be seen in Figs. 10(a3-f3). Similar phenomena can be found for $\arg(f_a)$ in xz -plane [Figs. 10(a1-f1)] and yz -plane [Figs. 10(a2-f2)].

B. Untie Three-twist knotted 5_2 EL configuration

Another case is to untie EL with the Three-twist knot 5_2 configuration. We start the tuning process with a EL exhibiting knot 5_2 structure (braid word $\sigma_1^{-1}\sigma_2\sigma_1^3\sigma_2$) obtain from Eq. (23) by setting $a = 1/4$. As shown in Fig. 7(a), the initial EL corresponds to a knot 5_2 embedded in stereographic coordinates. As shown in Fig. 7, by continuously increasing the width of braid trajectory a , the EL undergoes a series of topological transitions that effectively untie the knot through reconnection events, leading to unlinked ELs configurations. As a increase from 0.25, the first significant change occurs near $a \approx 0.43$, where two ECs form on each side of the σ_1^{-1} crossing [Fig. 7(b)]. The ECs are the intermediate states of the knot decomposition, causing the ELs to merge and alter the braid word to $\sigma_1^{-1}\sigma_1^3$, as depicted in the transition from Fig. 7(b) to Fig. 7(c). During this stage, the EL losses its knotted character and simplifies to a unentangled two-component configuration (Hopf linked ELs and unknotted ER).

Further increasing a to approximately 0.54 trigger a second reconnection, where the outer Hopf linked ELs near the former σ_1 crossings undergo another merging process [Fig. 7(d)]. The ECs in Fig. 7(d) transform the braid word into $\sigma_1\sigma_1^{-1}$, resulting in three fully unlinked ERs. For $a \geq 0.7$, as shown in Fig. 7(e), the ELs stabilize as three separate unknots, with the increased a only making that three ERs do not tangle and cannot change their unlinked ELs configurations, viewed down the z -axis from $(0, 0, \infty)$.

From a physical perspective, the process of untying knotted ELs via monotonic parameter increase establishes a deterministic and experimentally actionable pathway. The control parameter a can be directly linked to tunable experimental quantities, such as the strength of non-Hermitian gain/loss [65, 66] or the coupling coefficient in a synthetic dimension [67]. The underlying physical mechanism is that varying a governs the trajectories of the underlying EPs in parameter space. This EP dynamics drives a predetermined sequence of reconnection events for the ELs. In mathematical terms, these reconnections correspond to crossing changes; physically, they manifest as the merging, splitting, and reformation of non-Hermitian degeneracy lines in the system's spectrum.

Crucially, while both the Figure-eight 4_1 and the Three-twist 5_2 knots have a mathematical unknotting number of 1, indicating the existence of a theoretically minimal single-crossing-change path. Our method dictated path offers a deterministic, continuous, and universally applicable protocol. Although not necessarily minimal, this protocol is inherently more robust for experimental implementation. The entire process leaves clear spectra fingerprints, observable as the coales-

cence and separation of eigenvalue (real or imaginary parts) and the associated eigenstate braid [68].

VI. POSSIBLE ACOUSTIC REALIZATION

Our model is fundamentally characterized by the anti-Hermitian term d_I in the Hamiltonian Eq. (1), which introduces non-Hermitian effects essential for forming ELs. Compared to photonic [57] and cold-atom systems [58], acoustic systems combined with active electro-acoustic feedback offer a highly flexible route to engineering complex-valued and direction-dependent couplings [69–71]. Based on the theoretical framework in Sec. III, ELs with knotted or linked geometries can be implemented through designed acoustic resonator networks that emulate the non-Hermitian tight-binding Hamiltonian in Eqs. (C1–C3). A key experimental approach involves electro-acoustic coupling in Fig. (8) to break reciprocity, which is essential for stabilizing non-trivial EL configurations.

As shown schematically in Fig. (8), two acoustic cavities are each equipped with a microphone-speaker pair, allowing acoustic signals to be converted into electrical signals and re-injected into the opposite cavity after electronic processing. In the forward direction, the acoustic field detected in cavity 1 is amplified and phase shifted by an active circuit powered by a DC source, and subsequently drives the speaker in cavity 2. This process realizes an effective complex coupling coefficient $t_1 + i\delta_1$. In the backward direction, a distinct amplification-phase-shifting path is employed, leading to a generally different coupling $t_2 + i\delta_2$. Inequality $t_1 + i\delta_1 \neq t_2 + i\delta_2$ explicitly breaks reciprocity and gives rise to non-Hermitian, direction-dependent couplings between the two acoustic cavities.

In practice, a 3D lattice of such electro-acoustically coupled cavities can be constructed, with each unit cell implementing the same non-reciprocal coupling scheme. The control parameter a in Eq. (8), which determines the braid width and topology of ELs, can be tuned by adjusting the relative gain and phase offsets in the electronic feedback circuits. Experimental signatures of knotted or linked ELs may be detected through measurements of acoustic spectra, pressure distributions and phase responses using microphone arrays or laser vibrometry. Although challenges such as feedback stability and circuit-induced noise remain, the proposed electro-acoustic platform offers a scalable and experimentally accessible route for realizing nontrivial EL topologies in non-Hermitian acoustic systems.

VII. SUMMARY AND DISCUSSIONS

The results presented in this work establish knotted and linked exceptional loops (ELs) as a broadly accessible and systematically designable class of non-Hermitian band degeneracies. By constructing a universal, direct mapping from braid representations to minimal two-band non-Hermitian Hamiltonians, our framework elevates knot and link topology

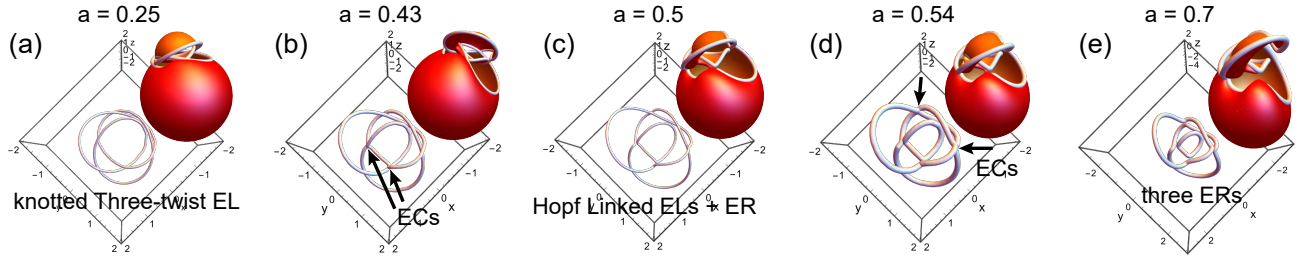


FIG. 7. The exceptional loops (ELs) obtained from Eq. (23) and their evolutions by continuously increasing scaling parameter a . Evolution of the morphology of ELs (main panels) and their Seifert surfaces (insets) by continuously increasing the scaling parameter a , starting from the knotted 5_2 EL with $a = 1/4$ in Fig. 7(a). The value of scaling parameter a is given in the top of each panel. The ELs configurations are labeled according to the context of the main text.

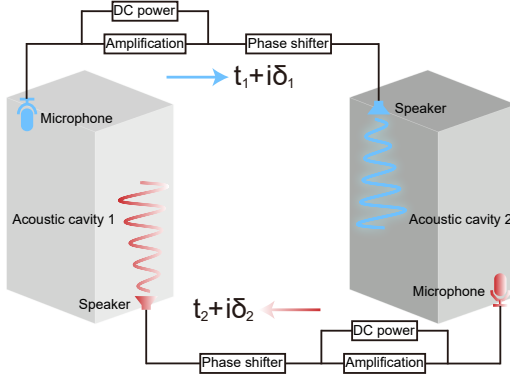


FIG. 8. Schematic of a nonreciprocal electro-acoustic coupling between two acoustic cavities. Each cavity is equipped with a microphone-speaker pair. The acoustic signal detected in cavity 1 is converted into an electrical signal, processed by amplification and phase-shifting circuits, and fed into cavity 2, resulting in a complex forward coupling $t_1 + i\delta_1$. Conversely, the signal propagating from cavity 2 to cavity 1 experiences a different amplification-phase-shifting path, giving rise to an unequal backward coupling $t_2 + i\delta_2$. The asymmetric signal processing breaks reciprocity and enables direction-dependent acoustic coupling.

from a model-dependent curiosity to a fundamental organizing principle for non-Hermitian band structures. This construction unifies all previously reported realizations of knotted and linked non-Hermitian degeneracies within a single theoretical pipeline [34–40] and, crucially, demonstrates that arbitrary knot and link topologies can be engineered without symmetry protection or fine-tuning. This generic stability constitutes a defining distinction between non-Hermitian exceptional degeneracies and their Hermitian counterparts—nodal lines and nodal chains—whose existence and classification are inherently tied to symmetry constraints [72–76].

A central conceptual insight of this work is that the topology of ELs is encoded in the global geometry of the degeneracy manifold, rather than in local topological charges that characterize Hermitian band topology. In stark contrast to Hermitian nodal lines, whose stability and topological classification rely on rigid symmetry constraints [77, 78], ELs

arise generically in 3D non-Hermitian systems as the intersection of real surfaces in momentum space. This intrinsic robustness frees EL topology from local symmetry requirements, enabling the realization of intricate knotted and linked configurations that are topologically forbidden or highly unnatural in Hermitian systems. From this perspective, classical knot invariants—including braid words, Alexander polynomials, and Seifert surfaces—acquire a direct physical interpretation as fundamental classifiers of non-Hermitian metallic phases, linking abstract topological mathematics to measurable spectral and structural properties of non-Hermitian matter. Our construction further unveils a deep, fundamental connection between non-Hermitian physics and classical knot theory, mediated by the use of semiholomorphic polynomials. These polynomials provide a natural, rigorous bridge between the algebraic description of knots and links in the three-sphere S^3 and their physical realization as ELs in Bloch momentum space. While polynomial constructions for knotted curves have long been a subject of pure mathematical inquiry, their embedding into non-Hermitian Hamiltonians reveals a broader principle: non-Hermitian systems act as a fertile experimental and theoretical arena where abstract topological objects can be directly encoded into experimentally observable spectral features. In this sense, knotted and linked ELs are not merely geometric curiosities but tangible physical realizations of mathematical knots, endowed with distinct observable consequences—including spectral winding, defective eigenstates, and non-Hermitian open Fermi surfaces bounded by the EL degeneracy manifold.

Beyond the static engineering of knotted EL topology, our demonstration of continuous untying of knotted ELs via a single tunable parameter introduces a new paradigm for topological manipulation in momentum space. Unlike Hermitian topological phase transitions, which are governed by gap closings at isolated high-symmetry points, the unknotting processes identified here proceed through deterministic, controlled reconnection events of exceptional points (EPs) and the transient generation of exceptional chains (ECs). ECs emerge as unavoidable intermediate states during EL untying, driving predictable morphological transformations of the degeneracy manifold without fine-tuning or symmetry breaking. These transitions establish a experimentally actionable route for al-

tering global knot topology in momentum space, and they suggest that knot complexity itself can be treated as a tunable physical resource in non-Hermitian systems. An intriguing open question that emerges from this work is whether distinct unknotting pathways are characterized by universal spectral or dynamical features, or whether material-specific and experimental dynamical constraints select preferred topological transition routes in realistic non-Hermitian platforms.

Several important and promising directions remain open for future exploration, building on the universal framework established here. First, while this work focuses on minimal two-band non-Hermitian models—the simplest platform for EL formation—extending the framework to multi-band non-Hermitian systems will likely unlock richer knotted and linked structures, enabled by higher-order exceptional degeneracies and nontrivial band permutations that have no two-band analogs. Second, the interplay between knotted ELs and additional symmetries—including crystalline, parity-time (PT), and non-Hermitian chiral symmetries—remains largely unexplored and may yield refined topological classification schemes, protected subclasses of knotted EL topology, or novel symmetry-enforced degeneracy transformations. Third, it would be of great fundamental and applied interest to investigate the dynamical and linear/nonlinear response phenomena associated with knotted ELs, including adiabatic encircling protocols [79, 80], nonreciprocal transport, non-Hermitian pumping [81], and the signatures of knotted topology in wave-packet evolution and nonlinear spectral response [82].

The universal framework developed herein extends far beyond the realm of non-Hermitian band theory, providing a general algorithm for engineering knotted topological structures that can serve as tailored initial conditions across diverse physical systems. The braid-based polynomial construction of knotted curves we introduce is broadly transferable, enabling the generation of knotted initial states for studying topological quantum dynamics in cold-atom and quantum optical systems [47], the design of knotted optical fields with bespoke phase singularities for topological photonics [44, 45], the investigation of knotted defect formation and evolution in liquid crystals and soft matter [83, 84], and the exploration of stable knotted solitons in classical and quantum field theories [85]. In this way, our work not only advances the understanding of non-Hermitian topological matter but also provides a cross-disciplinary tool for engineering knotted structures in physical science.

ACKNOWLEDGMENTS

This work was supported by the National Key R&D Program of China (2022YFA1404400), National Natural Science Foundation of China under grant Nos. 12125504 and 52306109, the CAS Pioneer Hundred Talents Program, Priority Academic Program Development (PAPD) of Jiangsu Higher Education Institutions, the Doctoral Support Program for Young Talents of the China Association for Science and Technology. We thank Han Zeng and Ruo-Yang Zhang for

useful discussion.

Appendix A: Seifert surface

A Seifert surface for a knot $\mathcal{K} \subset \mathcal{S}^3$ is a compact, connected, orientable surface S whose boundary is \mathcal{K} , *i.e.*, $\partial S = \mathcal{K}$. Its existence for any knot was established by Herbert Seifert in 1934 [88]. The standard constructive method, Seifert’s algorithm, begins with a regular projection of the knot. After assigning an orientation, all crossings are smoothed, with each crossing replaced by a non-crossing connection, thereby decomposing the diagram into disjoint simple closed curves called Seifert circles [89]. A disk is attached to each Seifert circle, and the original crossing information is restored by connecting the disks with twisted rectangular bands. The resulting surface is orientable and has the original knot as its boundary, though the construction is not unique.

An equivalent, more analytical description arises from considering a smooth, non-constant function $f_{\mathcal{K}} : \mathcal{S}^3 \setminus \mathcal{K} \rightarrow \mathbb{C}$ associated with the knot. If $f_{\mathcal{K}}$ extends suitably to a tubular neighbourhood of \mathcal{K} and its zero set meets the boundary of that neighbourhood precisely in \mathcal{K} , then for a regular value $\theta_0 \in [0, 2\pi)$ of the argument function, the pre-image

$$S_{\theta_0} = \{x \in \mathcal{S}^3 \setminus \mathcal{K} \mid \arg f_{\mathcal{K}}(x) = \theta_0\} \quad (\text{A1})$$

is also a compact, orientable surface bounded by \mathcal{K} . In this picture, the Seifert surfaces are the level sets of $\arg(f_{\mathcal{K}})$ providing a foliation of the knot complement by surfaces that share the common boundary \mathcal{K} . This viewpoint leads directly to the important class of fibered knots: when the map $f_{\mathcal{K}}/|f_{\mathcal{K}}| : \mathcal{S}^3 \setminus \mathcal{K} \rightarrow \mathcal{S}^1$ is a locally trivial fibration, its fibers are diffeomorphic Seifert surfaces, and the knot complement is a surface bundle over the circle. This connection makes Seifert surfaces a fundamental tool for studying the topology and dynamics of knot complements, including modern invariants in Heegaard Floer homology and contact geometry [90].

An essential invariant derived from any Seifert surface is its *genus*. The genus $g(\mathcal{K})$ of a knot is defined as the minimum genus among all Seifert surfaces for \mathcal{K} [91]; it is a knot invariant that distinguishes, for example, the unknot ($g = 0$) from the Trefoil knot ($g = 1$). Seifert surfaces also provide the geometric data for defining classical algebraic invariants. From a Seifert surface one constructs a Seifert matrix, a bilinear form whose symmetrisation yields the Alexander polynomial, and whose signature is the knot signature (see Appendix B B5). The minimal genus of a Seifert surface is closely related to the topological four-genus and appears naturally in the study of surfaces embedded in four-manifolds.

Standard examples include: the unknot, bounded by a disk [Fig. 9(a)]; the Trefoil knot [Fig. 9(b)], bounded by an orientable surface of genus 1, which can be visualized as a twisted band-and-disk arrangement homeomorphic to a punctured torus; and the Figure-eight knot [Fig. 9(c)], which also admits a genus-1 Seifert surface. Thus, Seifert surfaces, whether constructed combinatorially via Seifert’s algorithm or analytically as level sets of an argument function, offer a

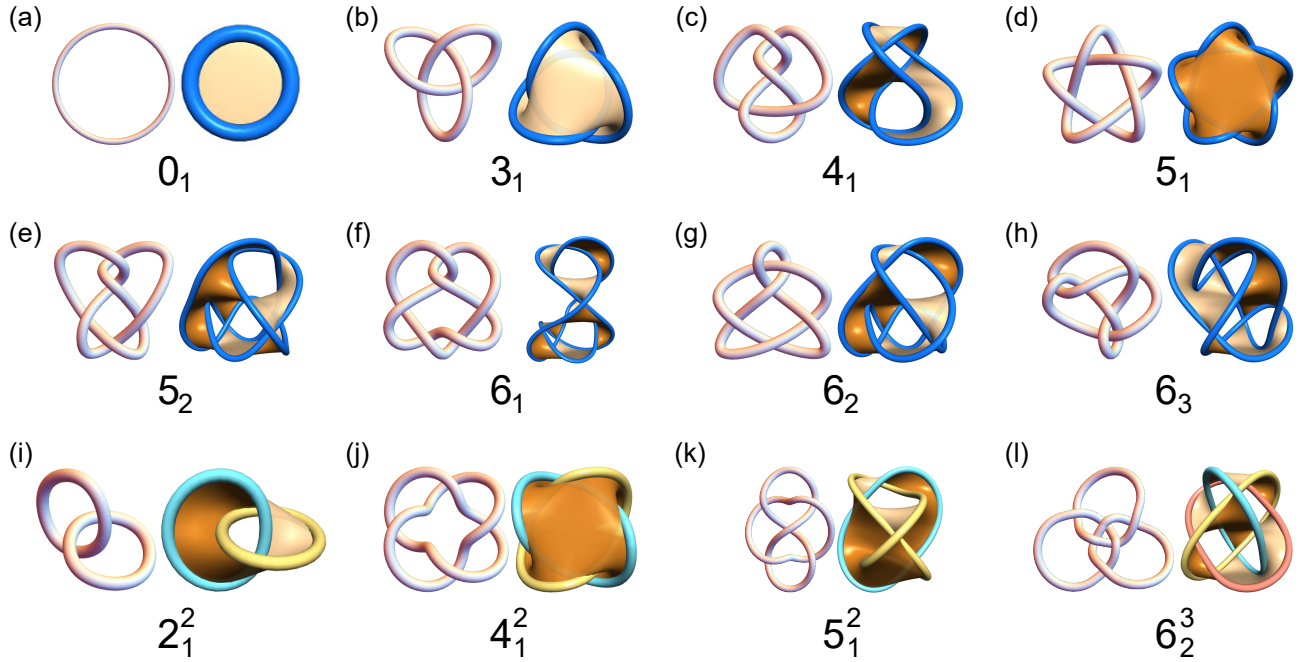


FIG. 9. A table of knot and link. (a-h) The Rolfsen table of knots with up to 6 crossings (left) and their corresponding Seifert surfaces (right). (i-l) The Rolfsen table of links (left) and their corresponding Seifert surfaces (right). All knots and links are plotted by *Wolfram Mathematica* 14 [86], and all Seifert surface are plotted by *Seifertview.exe* [87].

unifying geometric framework that links knot theory to low-dimensional topology, algebraic invariants, and the study of three- and four-dimensional manifolds.

Appendix B: Knot invariants

A knot is defined as an embedding of a circle S^1 into 3D space, typically taken as \mathbb{R}^3 or S^3 , while a link consists of multiple disjoint embedded circles. Two knots or links are considered equivalent if they can be continuously deformed into one another without cutting or self-intersection. A knot invariant is a quantity or algebraic object that remains unchanged under such ambient isotopies and therefore provides a means of distinguishing inequivalent knots or links.

In this work, knotted and linked ELs form extended degeneracy manifolds whose topology cannot be captured by local band indices alone. Knot invariants therefore play a central role as quantitative and algebraic tools for classifying and distinguishing inequivalent topological configurations. Different invariants probe complementary aspects of knot topology, ranging from polynomial characterizations of crossing structure to non-Abelian information encoded in the topology of the knot complement. In this section, we briefly review several knot invariants that are relevant to the classification of knotted ELs considered in the main text, including the Alexander polynomial, the Jones polynomial, the Conway polynomial, and the knot group.

B1. Alexander polynomial

We begin with the Alexander polynomial, one of the earliest and most widely used knot invariants, which assigns to each oriented knot or link \mathcal{K} a Laurent polynomial $\Delta_{\mathcal{K}}(t)$. Owing to its relatively simple structure and transparent formulation in terms of skein relations, the Alexander polynomial provides a natural starting point for the classification of knotted and linked ELs.

Consider three oriented links L_+ [Fig. 11(a)], L_- [Fig. 11(b)] and L_0 [Fig. 11(c)], which are identical except in a small neighborhood where they differ as follows: L_+ and L_- contain a positive and a negative crossing, respectively, while L_0 is obtained by performing the oriented smoothing of the crossing. The Alexander polynomial $\Delta_L(t)$ satisfies the skein relation [92]

$$\Delta_{L_+}(t) - \Delta_{L_-}(t) = (t^{1/2} - t^{-1/2})\Delta_{L_0}(t), \quad (\text{B1})$$

with the normalized condition

$$\Delta_{\text{unknot}}(t) = 1, \quad (\text{B2})$$

Together, these relations uniquely determine the Alexander polynomial for all knots and links, up to the conventional ambiguity $\Delta_L(t) \sim \pm t^n$.

We illustrate the skein-relation method by computing the Alexander polynomial of the trefoil knot 3_1 in a fully self-contained manner. Consider an oriented diagram of the trefoil knot and choose one of its crossings. Applying the skein

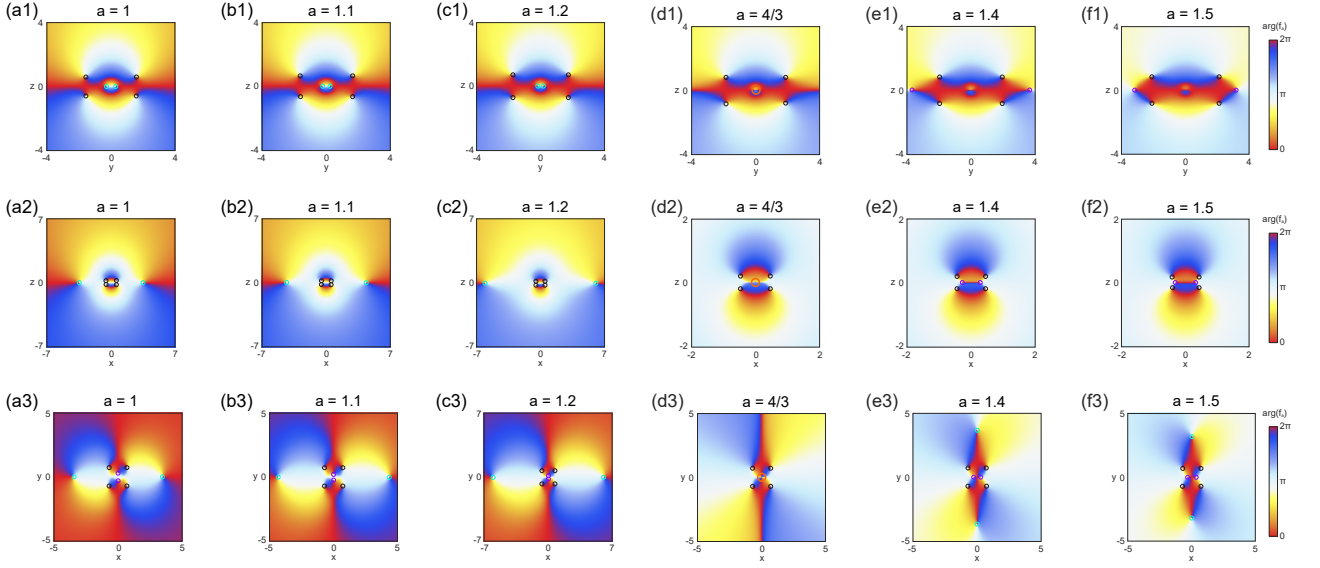


FIG. 10. The evolution of phase $\arg(f_a)$ obtain from Eq. (17) by continuously increasing scaling parameter a after performing the standard stereographic coordinates Eq. (32) in yz -plane (the first row), xz -plane (the second row) and xy -plane (the last row). Each vortex in $\arg(f_a)$ corresponds to an exceptional point, marked by circles. The value of a is given in the top of each panel. Panels (a3), (d3) and (f3) are selected into Figs. 6(d-f).

construction at this crossing produces three links: the original Trefoil L_+ , the diagram L_- obtained by reversing the crossing, and the smoothed diagram L_0 . For the trefoil, the crossing-reversed diagram L_- is isotopic to the unknot [see Fig. 11(e)], while the smoothed diagram L_0 is isotopic to the Hopf link [see Fig. 11(f)]. The skein relation then gives

$$\Delta_{\text{Trefoil}}(t) - \Delta_{\text{unknot}}(t) = (t^{1/2} - t^{-1/2})\Delta_{\text{Hopf}}(t). \quad (\text{B3})$$

Using the normalization $\Delta_{\text{unknot}}(t) = 1$, the computation of $\Delta_{\text{Trefoil}}(t)$ is reduced to determining the Alexander polynomial of the Hopf link. To compute $\Delta_{\text{Hopf}}(t)$, we apply the skein relation once more to a crossing of the Hopf link. In this case, the crossing-reversed diagram is isotopic to the two-component unlink [see Fig. 11(h)], while the smoothed diagram is isotopic to the unknot [see Fig. 11(i)]. The skein relation yields

$$\Delta_{\text{Hopf}}(t) - \Delta_{\text{unlink}}(t) = (t^{1/2} - t^{-1/2})\Delta_{\text{unknot}}(t). \quad (\text{B4})$$

Consequently, the Alexander polynomial of the Hopf link is given by

$$\Delta_{\text{Hopf}}(t) = t^{1/2} - t^{-1/2}. \quad (\text{B5})$$

Substituting Eq. (B5) into Eq. (B3), we obtain

$$\Delta_{\text{Trefoil}}(t) = t - 1 + t^{-1}. \quad (\text{B6})$$

Up to multiplication by $\pm t^n$, this is equivalent to the standard normalization

$$\Delta_{\text{Trefoil}}(t) = t^2 - t + 1, \quad (\text{B7})$$

which is the well-known Alexander polynomial of the trefoil knot.

The recursive structure of the skein relation makes the Alexander polynomial particularly suitable for systematically analyzing complex knot and link topologies by reducing them to simpler configurations. By iteratively applying the skein relation, the Alexander polynomials for other knots and links considered in the main text can be obtained in an analogous manner, as summarized in Table I. While the Alexander polynomial does not uniquely distinguish all knots, it provides a robust and computationally efficient invariant that captures the global structure of many knotted configurations realized in non-Hermitian band theory.

B2. Jones polynomial

The Jones polynomial is another powerful knot invariant, which assigns to each oriented knot or link \mathcal{K} a Laurent polynomial $V_{\mathcal{K}}(q)$ in a variable $q^{1/2}$. Unlike the Alexander polynomial, the Jones polynomial is sensitive to finer topological features and is capable of distinguishing certain knots that share the same Alexander polynomial.

The Jones polynomial is uniquely determined by the skein relation

$$q^{-1}V_{L_+}(q) - qV_{L_-}(q) = (q^{1/2} - q^{-1/2})V_{L_0}(q), \quad (\text{B8})$$

together with the Jones polynomial for N totally unlinked strings assigned to be

$$V_{\mathcal{O}}(q) = (-q^{-1/2} - q^{1/2})^{N-1}. \quad (\text{B9})$$

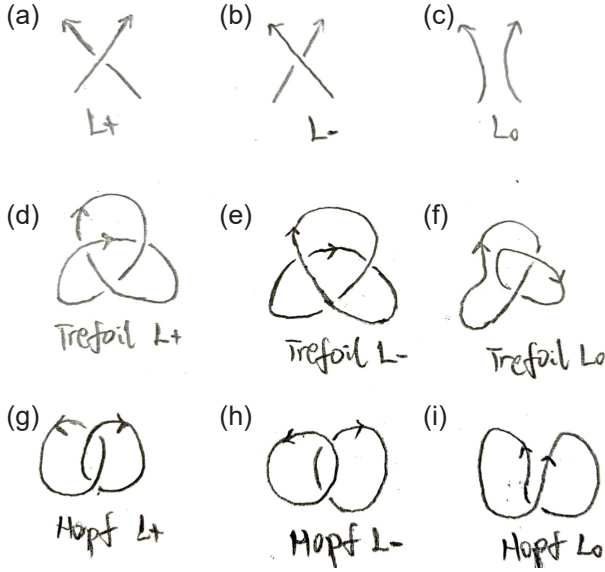


FIG. 11. Diagrammatic illustration of the skein relation. (a-c) Three oriented links showing the three local modifications at a crossing: the positive crossing L_+ in panel (a), the negative crossing L_- in panel (b), and the smoothed uncrossing L_0 in panel (c). The arrows indicate the oriented strands. (d-e) The result of applying the skein operation to a crossing of the trefoil knot. (g-i) The result of applying the skein operation to a crossing of the Hopf link.

Here L_+ , L_- , and L_0 again denote three oriented links that differ only in a small region containing a single crossing.

Starting from the unknot, the Jones polynomials of more complicated knots and links can be obtained recursively by iteratively applying the skein relation. In contrast to the Alexander polynomial, the Jones polynomial is not symmetric under $q \leftrightarrow q^{-1}$ and is capable of distinguishing certain knots that share the same Alexander polynomial. In this work, it serves as a complementary invariant for verifying and cross-checking the topology of knotted ELs constructed from braid representations.

B3. Conway polynomial

The Conway polynomial $\nabla_L(z)$ is a closely related knot invariant that can be viewed as a reparametrized version of the Alexander polynomial. It is defined through a simplified skein relation

$$\nabla_{L_+}(z) - \nabla_{L_-}(z) = z \nabla_{L_0}(z), \quad (\text{B10})$$

with the normalization

$$\nabla_{\text{unknot}}(z) = 1. \quad (\text{B11})$$

The Conway polynomial is related to the Alexander polynomial by a change of variables,

$$\Delta_L(t) = \nabla_L(t^{1/2} - t^{-1/2}), \quad (\text{B12})$$

up to normalization. This formulation often leads to simpler expressions and facilitates recursive computations using skein relations. While the Conway polynomial contains no more information than the Alexander polynomial, it provides a convenient alternative representation that emphasizes the local crossing structure of knots and links.

B4. Knot group

Polynomial invariants provide efficient algebraic characterizations of knot topology, but they necessarily compress the underlying topological information. A more complete invariant is given by the knot group, defined as the fundamental group of the complement of a knot or link [94],

$$G_{\mathcal{K}} = \pi_1(\mathcal{S}^3 \setminus \mathcal{K}). \quad (\text{B13})$$

The knot group encodes the global topological structure of how loops in space wind around the knot or link and provides a complete invariant up to mirror symmetry.

A standard presentation of the knot group is the Wirtinger presentation, which can be directly obtained from an oriented knot diagram. In this presentation, each arc of the diagram corresponds to a generator, while each crossing yields a relation expressing a conjugation between generators. The resulting group is generally non-Abelian and contains more topological information than polynomial invariants.

The Abelianization of the knot group recovers the first homology group of the knot complement [95],

$$G_{\mathcal{K}}^{\text{ab}} \cong H_1(\mathcal{S}^3 \setminus \mathcal{K}, \mathbb{Z}) \cong \mathbb{Z}, \quad (\text{B14})$$

which underlies the construction of the Alexander polynomial. In this sense, the Alexander polynomial may be viewed as an invariant derived from the Abelianized structure of the knot group, while the full knot group retains the complete non-Abelian topology.

In the context of non-Hermitian band theory, ELs act as branch-point singularities of the complex energy spectrum. Loops encircling these degeneracies exhibit nontrivial monodromy of eigenvalues and eigenstates, which is naturally characterized by the fundamental group of the complement of the ELs in momentum space [96–98]. The knot group therefore provides a natural topological framework for describing the global structure of knotted ELs and complements the polynomial invariants employed in this work.

B5. The relations between Seifert matrix and the Alexander polynomial

While the Alexander polynomial can be defined via skein relations, it also admits a concrete algebraic construction from the topology of a Seifert surface. This geometric perspective provides a direct link between the Alexander polynomial and the linking properties of curves on a Seifert surface, encoded in the Seifert matrix.

Name	Rolfen	braid	Alexander	Jones	Conway
Trefoil	3_1	σ_1^3	$1 - t + t^2$	$q + q^3 - q^4$	$1 + z^2$
Figure-eight	4_1	$(\sigma_1\sigma_2^{-1})^2$	$1 - 3t + t^2$	$q^{-2} - q^{-1} + 1 - q + q^2$	$1 - z^2$
Cinquefoil	5_1	σ_1^5	$1 - t + t^2 - t^3 + t^4$	$q^2 + q^4 - q^5 + q^6 - q^7$	$1 + 3z^2 + z^4$
Three-twist	5_2	$\sigma_1^{-1}\sigma_2\sigma_1^3\sigma_2$	$2 - 3t + 2t^2$	$q - q^2 + 2q^3 - q^4 + q^5 - q^6$	$1 + 2z^2$
Stevedore	6_1	$\sigma_1^2\sigma_2\sigma_1^{-1}\sigma_3^{-1}\sigma_2\sigma_3^{-1}$	$2 - 5t + 2t^2$	$q^{-2} - q^{-1} + 2 - 2q + q^2 - q^3 + q^4$	$1 - 2z^2$
Miller-Institute	6_2	$\sigma_1\sigma_2^{-1}\sigma_1^3\sigma_2^{-1}$	$1 - 3t + 3t^2 - 3t^3 + t^4$	$q^{-1} - 1 + 2q - 2q^2 + 2q^3 - 2q^4 + q^5$	$1 - z^2 - z^4$
	6_3	$(\sigma_1\sigma_3^{-1}\sigma_2\sigma_4^{-1})^2$	$1 - 3t + 5t^2 - 3t^3 + t^4$	$-q^{-3} + 2q^{-2} - 2q^{-1} + 3 - 2q + 2q^2 - q^3$	$1 + z^2 + z^4$
Hopf	$2_1^2(L2a1)$	σ_1^2		$-q - q^5$	z
Solomon	$4_1^2(L4a1)$	σ_1^4		$-q^3 - q^7 + q^9 - q^{11}$	$2z + z^3$
Whitehead	$5_1^2(L5a1)$	$\sigma_1\sigma_2^{-1}\sigma_1\sigma_2^{-1}\sigma_1$		$q^{-7} - 2q^{-5} + q^{-3} - 2q^{-1} + q - q^3$	z^3
Borromean	$6_2^3(L6a4)$	$(\sigma_1\sigma_2^{-1})^3$		$4 - q^{-6} + 3q^{-4} - 2q^{-2} - 2q^2 + 3q^4 - q^6$	z^4

TABLE I. Knots and Links and their braid words, Alexander polynomials, Jones polynomials and Conway polynomials. More knot/link invariants can be found in Ref. [93].

Let $\mathcal{K} \subset S^3$ be an oriented knot (or link) and S a connected, oriented Seifert surface for \mathcal{K} (as constructed in Appendix A). Denote by g the genus of S , and choose a basis $\{a_1, b_1, \dots, a_g, b_g\}$ for the first homology group $H_1(S, \mathbb{Z}) \cong \mathbb{Z}^{2g}$, represented by oriented simple closed curves on S that are disjoint except for a single transverse intersection point between a_i and b_i .

For a curve $\alpha \subset S$, let α^+ denote a push-off of α in the positive normal direction of S (determined by the orientation of S and the orientation of \mathbb{R}^3). The *Seifert form* is the bilinear form

$$\ell : H_1(S, \mathbb{Z}) \times H_1(S, \mathbb{Z}) \longrightarrow \mathbb{Z} \quad (\text{B15})$$

defined by $\ell(\alpha, \beta^+)$, the linking number of α with the positively pushed-off copy of β . The *Seifert matrix* V (with respect to the chosen basis) is the $2g \times 2g$ integer matrix with entries

$$V_{ij} = \ell(\gamma_i, \gamma_j), \quad \gamma_1, \dots, \gamma_{2g} = a_1, b_1, \dots, a_g, b_g. \quad (\text{B16})$$

The Seifert matrix depends on the choice of Seifert surface and the basis, but its equivalence class under certain moves (S -equivalence) is a knot invariant.

The Alexander polynomial $\Delta_{\mathcal{K}}(t)$ can be expressed in terms of any Seifert matrix V as [99]

$$\Delta_{\mathcal{K}}(t) = \det(V - tV^T), \quad (\text{B17})$$

up to multiplication by $\pm t^n$ (the usual normalization ambiguity). This determinant is a Laurent polynomial in $t^{1/2}$ that is symmetric under $t \leftrightarrow t^{-1}$ after appropriate normalization.

For the trefoil knot 3_1 , a genus-one Seifert surface can be taken as a once-punctured torus. Choosing canonical curves a (meridian) and b (longitude) on the torus with algebraic intersection $a \bullet b = 1$, and computing linking numbers of pushed-off copies, one obtains the Seifert matrix

$$V = \begin{pmatrix} 1 & 0 \\ 1 & -1 \end{pmatrix}. \quad (\text{B18})$$

Then

$$\det(V - tV^T) = \begin{vmatrix} 1-t & -t \\ 1 & -1+t \end{vmatrix} = t^2 - t + 1, \quad (\text{B19})$$

which matches the Alexander polynomial of the Trefoil given in Table I.

The Seifert matrix also yields other classical invariants. The symmetrization $V + V^T$ is the intersection matrix of the Seifert surface, whose signature is the *knot signature* $\sigma(\mathcal{K})$. Moreover, the determinant of the knot is given by $|\Delta_{\mathcal{K}}(-1)| = \det(V + V^T)$.

Thus, the Seifert matrix provides a unified geometric framework that connects the topology of a Seifert surface to the Alexander polynomial and other classical knot invariants. While the Seifert matrix itself is not a knot invariant (it depends on the choice of Seifert surface), the S -equivalence class of Seifert matrices completely determines the Alexander polynomial and the knot signature, illustrating the deep interplay between the geometry of Seifert surfaces and the algebra of knot invariants.

Appendix C: Hamiltonian for tight-binding models

For the Trefoil knot [3₁ in the Rolfsen's table, Torus knot $T(2, 3)$], we impose $f_1 + if_2 = u^2 + v^3$, then we obtain

$$\begin{aligned}
 f_1 &= \left(\frac{3}{2}P^2 + Q^2 - \frac{1}{2}\right) + \frac{P^2}{2}\cos(2k_\alpha) + \frac{1}{2}\cos(2k_z) - 2PQ\cos(k_\alpha) + P^2\cos(k_\alpha \pm k_\beta) \\
 &\quad - \frac{1}{4}\sin(3k_x) + \frac{3}{4}\sin(k_x \pm 2k_y) - \frac{3}{4}\sin(k_x), \\
 f_2 &= \frac{1}{4}\sin(3k_y) + \frac{3}{4}\sin(k_y) + P\sin(2k_z) - 2Q\sin(k_z) - \frac{3}{4}[\sin(2k_x + k_y) - \sin(2k_x - k_y)] \\
 &\quad + P[\sin(k_x + k_z) - \sin(k_x - k_z) + \sin(k_y + k_z) - \sin(k_y - k_z)],
 \end{aligned} \tag{C1}$$

where k_α means sum over $\alpha = x, y, z$, and $k_\alpha \pm k_\beta$ means sum over $\alpha\beta = xy, yz, zx$.

For the Hopf Link [2₁² in the Rolfsen's table of link and $L2a1$ in the Thistlethwaite's link table, Torus knot $T(2, 2)$], we impose $f_1 + if_2 = u^2 + v^2$, then we obtain

$$\begin{aligned}
 f_1 &= \left(\frac{3}{2}P^2 + Q^2 - \frac{1}{2}\right) + \frac{P^2}{2}\cos(2k_\alpha) + \frac{1}{2}[-\cos(2k_x) + \cos(2k_y) + \cos(2k_z)] - 2PQ\cos(k_\alpha) + P^2\cos(k_\alpha \pm k_\beta), \\
 f_2 &= P\sin(2k_z) - 2Q\sin(k_z) + P[\sin(k_x + k_z) - \sin(k_x - k_z) + \sin(k_y + k_z) - \sin(k_y - k_z)] \\
 &\quad + [\cos(k_x - k_y) - \cos(k_x + k_y)].
 \end{aligned} \tag{C2}$$

For the Figure-eight knot [4₁ in the Rolfsen's table, Lemniscate knot $L(2, 3, 2)$], we substitute Eq. (17) into Eq. (8), then we obtain

$$\begin{aligned}
 f_1 &= (96P + 36a^2Q - 64P^3 - 288QP^2) + 16P^3\cos(3k_\alpha) - 96QP^2\cos(2k_\alpha) + [14a^3\cos(2k_x) - 14a^3\cos(2k_y) \\
 &\quad - 96Q\cos(2k_z)] + (240P^3 + 192Q^2P - 36a^2P - 96P)\cos(k_\alpha) + 48P\cos(k_\alpha \pm 2k_z) + 48P^3[\cos(k_\alpha \pm 2k_\beta) \\
 &\quad + \cos(2k_\alpha \pm k_\beta)] - 192QP^2\cos(k_\alpha \pm k_\beta) + 96P^3\cos(k_x \pm k_y \pm k_z) + 24a^2[\sin(k_x + k_y + k_z) \\
 &\quad + \sin(k_x - k_y - k_z) - \sin(k_x + k_y - k_z) - \sin(k_x - k_y + k_z)], \\
 f_2 &= 16\sin(3k_z) + (288P^2 + 192Q^2 - 36a^2 - 48)\sin(k_z) + 48P^2[\sin(2k_\alpha + k_z) - \sin(2k_\alpha - k_z)] \\
 &\quad + 96P^2[\sin(k_x + 2k_z) - \sin(k_x - 2k_z) + \sin(k_y + 2k_z) - \sin(k_y - 2k_z)] + 96P^2[\sin(k_x \pm k_y + k_z) \\
 &\quad - \sin(k_x \pm k_y - k_z)] - 192PQ[\sin(k_\alpha + k_z) - \sin(k_\alpha - k_z)] + a^3[\cos(k_x - 3k_y) - \cos(k_x + 3k_y) \\
 &\quad + \cos(3k_x + k_y) - \cos(3k_x - k_y)] + 24a^2P[\cos(k_x - 2k_y) - \cos(k_x + 2k_y) + \cos(2k_x - k_y) - \cos(2k_x + k_y)] \\
 &\quad + 24a^2P[\cos(k_x - k_y \pm k_z) - \cos(k_x + k_y \pm k_z)] - 48a^2Q[\cos(k_x - k_y) - \cos(k_x + k_y)].
 \end{aligned} \tag{C3}$$

The corresponding tight-binding model is then obtained by inserting f_1 and f_2 into Eqs. (1-3). The constructive approach is general and can be similarly applied to derive tight-binding models for other complex knotted and linked ELs. The degree of the semiholomorphic function $F_a(u, v, \bar{v})$, defined as the maximum sum of the exponents of u , v and \bar{v} in each term of the polynomial, dictates the maximum range of hopping in the tight-binding model. For example, for the Trefoil knot with $F_a = u^2 + v^3$, the degree is 3, leading to the third-nearest-neighbor couplings. Similarly, for the Hopf link with $F_a = u^2 + v^2$, only leading to next-nearest-neighbor couplings. Thus, the longer hopping in the non-Hermitian systems can induce more intricate and complex morphology of ELs.

-
- [1] W. D. Heiss, "Exceptional points of non-hermitian operators," *J. Phys. A: Math. Gen.* **37**, 2455 (2004).
- [2] R. El-Ganainy and K. G. Makris, M. Khajavikhan, Z. H. Muslimani, S. Rotter, and D. N. Christodoulides, "Non-hermitian physics and pt symmetry," *Nat. Phys.* **14**, 11–19 (2018).
- [3] Y. Ashida, Z. Gong, and M. Ueda, "Non-hermitian physics," *Adv. Phys.* **69**, 249–435 (2020).
- [4] E. J. Bergholtz, J. C. Budich, and F. K. Kunst, "Exceptional topology of non-hermitian systems," *Rev. Mod. Phys.* **93**, 015005 (2021).
- [5] L. Feng, R. El-Ganainy, and L. Ge, "Non-hermitian photonics based on parity–time symmetry," *Nat. Photonics* **11**, 752–762 (2017).
- [6] M. Pan, H. Zhao, P. Miao, S. Longhi, and L. Feng, "Photonic zero mode in a non-hermitian photonic lattice," *Nat. Commun.* **9**, 1308 (2018).
- [7] M.-A. Miri and A. Alu, "Exceptional points in optics and photonics," *Science* **363**, eaar7709 (2019).
- [8] A. Li, H. Wei, M. Cotrufo, W. Chen, S. Mann, X. Ni, B. Xu, J. Chen, J. Wang, S. Fan, *et al.*, "Exceptional points and non-

- hermitian photonics at the nanoscale,” *Nat. Nanotechnol.* **18**, 706–720 (2023).
- [9] X. Feng, T. Wu, Z. Gao, H. Zhao, S. Wu, Y. Zhang, L. Ge, and L. Feng, “Non-hermitian hybrid silicon photonic switching,” *Nat. Photonics* **19**, 264–270 (2025).
- [10] L. Xiao, K. Wang, D. Qu, H. Gao, Q. Lin, Z. Bian, X. Zhan, and P. Xue, “Non-hermitian physics in photonic systems,” *Photon. Insights* **4**, R09–R09 (2025).
- [11] H. Gao, H. Xue, Z. Gu, T. Liu, J. Zhu, B. Zhang, *et al.*, “Non-hermitian route to higher-order topology in an acoustic crystal,” *Nat. Commun.* **12**, 1888 (2021).
- [12] Q. Zhang, Y. Li, H. Sun, X. Liu, L. Zhao, X. Feng, X. Fan, and C. Qiu, “Observation of acoustic non-hermitian bloch braids and associated topological phase transitions,” *Phys. Rev. Lett.* **130**, 017201 (2023).
- [13] L. Huang, S. Huang, C. Shen, S. Yves, A. S. Pilipchuk, X. Ni, S. Kim, Y. K. Chiang, D. A. Powell, J. Zhu, *et al.*, “Acoustic resonances in non-hermitian open systems,” *Nat. Rev. Phys.* **6**, 11–27 (2024).
- [14] T. Yoshida and Y. Hatsugai, “Exceptional rings protected by emergent symmetry for mechanical systems,” *Phys. Rev. B* **100**, 054109 (2019).
- [15] X. Cui, R.-Y. Zhang, X. Wang, W. Wang, G. Ma, and C. T. Chan, “Experimental realization of stable exceptional chains protected by non-hermitian latent symmetries unique to mechanical systems,” *Phys. Rev. Lett.* **131**, 237201 (2023).
- [16] X.-X. Zhang and M. Franz, “Non-hermitian exceptional landau quantization in electric circuits,” *Phys. Rev. Lett.* **124**, 046401 (2020).
- [17] X. Zhou, W. Zhang, W. Cao, and X. Zhang, “Non-hermitian floquet topological sensors for ultrasensitive detection of dynamic signals,” *Phys. Rev. Lett.* **135**, 106601 (2025).
- [18] K. Sone, Y. Ashida, and T. Sagawa, “Exceptional non-hermitian topological edge mode and its application to active matter,” *Nat. Commun.* **11**, 5745 (2020).
- [19] K. Sone, K. Yokomizo, K. Kawaguchi, and Y. Ashida, “Hermitian and non-hermitian topology in active matter,” *Rep. Prog. Phys.* (2025).
- [20] A. Li, J. Dong, J. Wang, Z. Cheng, J. S. Ho, D. Zhang, J. Wen, X.-L. Zhang, C. T. Chan, A. Alù, *et al.*, “Hamiltonian hopping for efficient chiral mode switching in encircling exceptional points,” *Phys. Rev. Lett.* **125**, 187403 (2020).
- [21] K. Li, H. Peng, S. Wang, Q. Yi, L. Chen, Y. Zhang, J. Zeng, and J. Wang, “High-performance chiral mode switching devices using silicon metamaterial waveguides beyond $1.55 \mu\text{m}$,” *Laser Photonics Rev.* **19**, 2401344 (2025).
- [22] A. Laha, S. Dey, H. K. Gandhi, A. Biswas, and S. Ghosh, “Exceptional point and toward mode-selective optical isolation,” *ACS photonics* **7**, 967–974 (2020).
- [23] Y. S. S. Patil, J. Höller, P. A. Henry, C. Guria, Y. Zhang, L. Jiang, N. Kralj, N. Read, and J. G. E. Harris, “Measuring the knot of non-hermitian degeneracies and non-commuting braids,” *Nature* **607**, 271–275 (2022).
- [24] C. Guria, Q. Zhong, S. K. Ozdemir, Y. S. S. Patil, R. El-Ganainy, and J. G. E. Harris, “Resolving the topology of encircling multiple exceptional points,” *Nat. Commun.* **15**, 1369 (2024).
- [25] M. Parto, C. Leefmans, J. Williams, R. M. Gray, and A. Marandi, “Enhanced sensitivity via non-hermitian topology,” *Light Sci. Appl.* **14**, 6 (2025).
- [26] S.-X. Wang and Z. Yan, “Enhanced sensitivity in non-hermitian systems at infernal points,” *Phys. Rev. Res.* **7**, L022037 (2025).
- [27] S. Lin, L. Jin, and Z. Song, “Symmetry protected topological phases characterized by isolated exceptional points,” *Phys. Rev. B* **99**, 165148 (2019).
- [28] W. Cao, W. Zhang, and X. Zhang, “Observation of knot topology of exceptional points,” *Phys. Rev. B* **109**, 165128 (2024).
- [29] H. Zhou, C. Peng, Y. Yoon, C. W. Hsu, K. A. Nelson, L. Fu, J. D. Joannopoulos, M. Soljačić, and B. Zhen, “Observation of bulk fermi arc and polarization half charge from paired exceptional points,” *Science* **359**, 1009–1012 (2018).
- [30] J. Hu, R.-Y. Zhang, M. Wang, D. Wang, S. Ma, J. Huang, L. Wang, X. Ouyang, Y. Zhu, H. Jia, *et al.*, “Unconventional bulk-fermi-arc links paired third-order exceptional points splitting from a defective triple point,” *Commun. Phys.* **8**, 90 (2025).
- [31] Y. Xu, S.-T. Wang, and L.-M. Duan, “Weyl exceptional rings in a three-dimensional dissipative cold atomic gas,” *Phys. Rev. Lett.* **118**, 045701 (2017).
- [32] R.-Y. Zhang, X. Cui, W.-J. Chen, Z.-Q. Zhang, and C. T. Chan, “Symmetry-protected topological exceptional chains in non-hermitian crystals,” *Commun. Phys.* **6**, 169 (2023).
- [33] W. Zhang, H. Yuan, W. Cao, and X. Zhang, “Exploring four-dimensional topological manifolds of non-hermitian bands from klein bottles to spun trefoil knots,” *Phys. Rev. B* **110**, 224108 (2024).
- [34] J. Carlström, M. Stålhammar, J. C. Budich, and E. J. Bergholtz, “Knotted non-hermitian metals,” *Phys. Rev. B* **99**, 161115 (2019).
- [35] X. Zhang, G. Li, Y. Liu, T. Tai, R. Thomale, and C. H. Lee, “Tidal surface states as fingerprints of non-hermitian nodal knot metals,” *Commun. Phys.* **4**, 47 (2021).
- [36] K. Wang, L. Xiao, J. C. Budich, W. Yi, and P. Xue, “Simulating exceptional non-hermitian metals with single-photon interferometry,” *Phys. Rev. Lett.* **127**, 026404 (2021).
- [37] J. Carlström and E. J. Bergholtz, “Exceptional links and twisted fermi ribbons in non-hermitian systems,” *Phys. Rev. A* **98**, 042114 (2018).
- [38] Z. Yang and J. Hu, “Non-hermitian hopf-link exceptional line semimetals,” *Phys. Rev. B* **99**, 081102 (2019).
- [39] Z. Zhang, Z. Yang, and J. Hu, “Bulk-boundary correspondence in non-hermitian hopf-link exceptional line semimetals,” *Phys. Rev. B* **102**, 045412 (2020).
- [40] P. He, J.-H. Fu, D.-W. Zhang, and S.-L. Zhu, “Double exceptional links in a three-dimensional dissipative cold atomic gas,” *Phys. Rev. A* **102**, 023308 (2020).
- [41] T. Machon and G. P. Alexander, “Knotted defects in nematic liquid crystals,” *Phys. Rev. Lett.* **113**, 027801 (2014).
- [42] H. Zhang, W. Zhang, Y. Liao, X. Zhou, J. Li, G. Hu, and X. Zhang, “Creation of acoustic vortex knots,” *Nat. Commun.* **11**, 3956 (2020).
- [43] M. R. Dennis, R. P. King, B. Jack, K. O’holleran, and M. J. Padgett, “Isolated optical vortex knots,” *Nat. Phys.* **6**, 118–121 (2010).
- [44] Z. Wang, X. Lu, Z. Chen, Y. Cai, and C. Zhao, “Topological links and knots of speckled light mediated by coherence singularities,” *Light Sci. Appl.* **14**, 1–9 (2025).
- [45] Q. Wang, C. Tu, X. Zhang, Y. Li, J.-H. Zhao, M.-Y. Wang, Y. Li, and H.-T. Wang, “Topological encryption enabled by longitudinal component of structured light field,” *Adv. Photonics* **8**, 016003–016003 (2026).
- [46] Z. Zhang, L. Li, Y. Zhu, R. Zhang, M. Yang, and L. Dai, “Behavior of active polymer knots,” *Macromolecules* **58**, 11229–11236 (2025).
- [47] D. S. Hall, M. W. Ray, K. Tiurev, E. Ruokokoski, A. H. Georghge, and M. Möttönen, “Tying quantum knots,” *Nat. Phys.* **12**, 478–483 (2016).
- [48] M. Eto, Y. Hamada, and M. Nitta, “Tying knots in particle physics,” *Phys. Rev. Lett.* **135**, 091603 (2025).

- [49] N. A. Veretenov, S. V. Fedorov, and N. N. Rosanov, “Topological vortex and knotted dissipative optical 3d solitons generated by 2d vortex solitons,” *Phys. Rev. Lett.* **119**, 263901 (2017).
- [50] M. Stålhammar, L. Rødland, G. Arone, J. C. Budich, and E. Bergholtz, “Hyperbolic nodal band structures and knot invariants,” *SciPost Phys.* **7**, 019 (2019).
- [51] J. W. Alexander, “A lemma on systems of knotted curves,” *Proc. Natl. Acad. Sci.* **9**, 93–95 (1923).
- [52] V. O. Manturov, *Knot theory* (CRC press, 2018).
- [53] T. A. Gittings, “Minimum braids: a complete invariant of knots and links,” *arXiv preprint math/0401051* (2004).
- [54] M. R. Dennis and B. Bode, “Constructing a polynomial whose nodal set is the three-twist knot 52,” *J. Phys. A: Math. Theor.* **50**, 265204 (2017).
- [55] B. Bode and M. R. Dennis, “Constructing a polynomial whose nodal set is any prescribed knot or link,” *J. Knot Theory Ramifications* **28**, 1850082 (2019).
- [56] H. Hu and E. Zhao, “Knots and non-hermitian bloch bands,” *Phys. Rev. Lett.* **126**, 010401 (2021).
- [57] Y. Zhang, X. Dai, and Y. Xiang, “Topological hierarchy in non-hermitian three-dimensional photonic crystals,” *Phys. Rev. B* **110**, 104103 (2024).
- [58] E. Zhao, Z. Wang, C. He, T. F. J. Poon, K. K. Pak, Y.-J. Liu, P. Ren, X.-J. Liu, and G.-B. Jo, “Two-dimensional non-hermitian skin effect in an ultracold fermi gas,” *Nature* **637**, 565–573 (2025).
- [59] H. Park, W. Gao, X. Zhang, and S. S. Oh, “Nodal lines in momentum space: topological invariants and recent realizations in photonic and other systems,” *Nanophotonics* **11**, 2779–2801 (2022).
- [60] V. I. Arnold, *Singularity theory*, Vol. 53 (Cambridge University Press, 1981).
- [61] P. B. Kronheimer and T. S. Mrowka, “Gauge theory for embedded surfaces. i,” *Topology* **32**, 773–826 (1993).
- [62] P. Ozsváth and Z. Szabó, “Holomorphic disks and knot invariants,” *Adv. Math.* **186**, 58–116 (2004).
- [63] T. Applebaum, S. Blackwell, A. Davies, T. Edlich, A. Juhász, M. Lackenby, N. Tomašev, and D. Zheng, “The unknotting number, hard unknot diagrams, and reinforcement learning,” *arXiv preprint 2409.09032* (2024).
- [64] P. B. Kronheimer and T. S. Mrowka, “Gauge theory and rasmussen’s invariant,” *J. Topol.* **6**, 659–674 (2013).
- [65] W.-C. Jiang, H. Wu, Q.-X. Li, J. Li, and J.-J. Zhu, “Tunable non-hermitian skin effect via gain and loss,” *Phys. Rev. B* **110**, 155144 (2024).
- [66] A. Hashemi, E. L. Pereira, H. Li, J. L. Lado, and A. Blanco-Redondo, “Observation of non-hermitian topology from optical loss modulation,” *Nat. Mater.* **24**, 1393–1399 (2025).
- [67] A. Dutt, Q. Lin, L. Yuan, M. Minkov, M. Xiao, and S. Fan, “A single photonic cavity with two independent physical synthetic dimensions,” *Science* **367**, 59–64 (2020).
- [68] K. Wang, A. Dutt, C. C. Wojcik, and S. Fan, “Topological complex-energy braiding of non-hermitian bands,” *Nature* **598**, 59–64 (2021).
- [69] L. Zhang, Y. Yang, Y. Ge, Y.-J. Guan, Q. Chen, Q. Yan, F. Chen, R. Xi, Y. Li, D. Jia, *et al.*, “Acoustic non-hermitian skin effect from twisted winding topology,” *Nat. Commun.* **12**, 6297 (2021).
- [70] Z. Gu, H. Gao, H. Xue, J. Li, Z. Su, and J. Zhu, “Transient non-hermitian skin effect,” *Nat. Commun.* **13**, 7668 (2022).
- [71] B.-B. Wang, Z. Cheng, H.-Y. Zou, Y. Ge, K.-Q. Zhao, Q.-R. Si, S.-Q. Yuan, H.-X. Sun, H. Xue, and B. Zhang, “Observation of disorder-induced boundary localization,” *Proc. Natl. Acad. Sci.* **122**, e2422154122 (2025).
- [72] A. A. Burkov, M. D. Hook, and L. Balents, “Topological nodal semimetals,” *Phys. Rev. B* **84**, 235126 (2011).
- [73] Z. Yan, R. Bi, H. Shen, L. Lu, S.-C. Zhang, and Z. Wang, “Nodal-link semimetals,” *Phys. Rev. B* **96**, 041103 (2017).
- [74] Y. Zhou, F. Xiong, X. Wan, and J. An, “Hopf-link topological nodal-loop semimetals,” *Phys. Rev. B* **97**, 155140 (2018).
- [75] T. Bzduszek, Q. Wu, A. Rüegg, M. Sigrist, and A. A. Soluyanov, “Nodal-chain metals,” *Nature* **538**, 75–78 (2016).
- [76] Q. Yan, R. Liu, Z. Yan, B. Liu, H. Chen, Z. Wang, and L. Lu, “Experimental discovery of nodal chains,” *Nat. Phys.* **14**, 461–464 (2018).
- [77] C.-K. Chiu, Jeffrey C. Y. Teo, A. P. Schnyder, and S. Ryu, “Classification of topological quantum matter with symmetries,” *Rev. Mod. Phys.* **88**, 035005 (2016).
- [78] H.-C. Po, A. Vishwanath, and H. Watanabe, “Symmetry-based indicators of band topology in the 230 space groups,” *Nat. Commun.* **8**, 50 (2017).
- [79] J. Feilhauer, A. Schumer, J. Doppler, A. A. Mailybaev, J. Böhm, U. Kuhl, N. Moiseyev, and S. Rotter, “Encircling exceptional points as a non-hermitian extension of rapid adiabatic passage,” *Phys. Rev. A* **102**, 040201 (2020).
- [80] I. I. Arkhipov, A. Miranowicz, F. Minganti, Ş. K. Özdemir, and F. Nori, “Dynamically crossing diabolic points while encircling exceptional curves: A programmable symmetric-asymmetric multimode switch,” *Nat. Commun.* **14**, 2076 (2023).
- [81] C. H. Lee, L. Li, R. Thomale, and J. Gong, “Unraveling non-hermitian pumping: Emergent spectral singularities and anomalous responses,” *Phys. Rev. B* **102**, 085151 (2020).
- [82] Y. Zheng, K. Pu, L. Ren, C. Bai, and Z. Liang, “Nonreciprocity induced fractional nonlinear thouless pumping,” *arXiv preprint 2602.02102* (2026).
- [83] P. J. Ackerman and I. I. Smalyukh, “Diversity of knot solitons in liquid crystals manifested by linking of preimages in torons and hopfions,” *Phys. Rev. X* **7**, 011006 (2017).
- [84] D. Hall, J.-S. B. Tai, L. H. Kauffman, and I. I. Smalyukh, “Fusion and fission of particle-like chiral nematic vortex knots,” *Nat. Phys.* , 1–9 (2025).
- [85] Y. Amari and N. Sawado, “Su(3) knot solitons: Hopfions in the f2 skyrme–faddeev–niemi model,” *Phys. Lett. B* **784**, 294–300 (2018).
- [86] “<https://reference.wolfram.com/language/ref/knotdata.html>,” .
- [87] “<https://vanwijk.win.tue.nl/seifertview/>,” .
- [88] H. Seifert, “Über das geschlecht von knoten,” *Math. Ann.* **110**, 571–592 (1935).
- [89] D. Rolfsen, *Knots and links*, 346 (American Mathematical Soc., 2003).
- [90] Y. Ni, “Knot floer homology detects fibred knots,” *Invent. Math.* **170**, 577–608 (2007).
- [91] W. R. Lickorish, *An introduction to knot theory*, Vol. 175 (Springer Science & Business Media, 2012).
- [92] Z. Yang, “Knot invariants with multiple skein relations,” *J. Knot Theory Ramifications* **27**, 1850017 (2018).
- [93] “<https://linkinfo.knotinfo.org/>,” .
- [94] C. McA. Gordon and J. Luecke, “Knots are determined by their complements,” *J. Amer. Math. Soc.* , 371–415 (1989).
- [95] M. López Hernández, “Knowing a knot from the abelianization of its fundamental group on s3,” *J. Adv. Stud. Topol.* **13** (2023).
- [96] C. C. Wojcik, X.-Q. Sun, T. Bzduszek, and S. Fan, “Homotopy characterization of non-hermitian hamiltonians,” *Phys. Rev. B* **101**, 205417 (2020).
- [97] Z. Li and R. S. K. Mong, “Homotopical characterization of non-hermitian band structures,” *Phys. Rev. B* **103**, 155129 (2021).
- [98] C. C. Wojcik, K. Wang, A. Dutt, J. Zhong, and S. Fan, “Eigenvalue topology of non-hermitian band structures in two and

- three dimensions,” *Phys. Rev. B* **106**, L161401 (2022).
- [99] J. Collins, “An algorithm for computing the seifert matrix of a link from a braid representation,” *Ensaio Matemáticos* **30**, 246 (2016).